Volume 1 | Number 1 | Jan 2013 | Pages 1–100

PCCP

Physical Chemistry Chemical Physics
www.rsc.org/pccp

ROYAL SOCIETY OF CHEMISTRY

This is an *Accepted Manuscript*, which has been through the Royal Society of Chemistry peer review process and has been accepted for publication.

Accepted Manuscripts are published online shortly after acceptance, before technical editing, formatting and proof reading. Using this free service, authors can make their results available to the community, in citable form, before we publish the edited article. We will replace this *Accepted Manuscript* with the edited and formatted *Advance Article* as soon as it is available.

You can find more information about *Accepted Manuscripts* in the **Information for Authors**.

Please note that technical editing may introduce minor changes to the text and/or graphics, which may alter content. The journal's standard **Terms & Conditions** and the **Ethical guidelines** still apply. In no event shall the Royal Society of Chemistry be held responsible for any errors or omissions in this *Accepted Manuscript* or any consequences arising from the use of any information it contains.

Analysis of the structure of nanocomposites of triglyceride platelets and DNA

Martin Schmiele, Charlotte Knittel, Tobias Unruh [*]

Sebastian Busch [†]   Humphrey Morhenn [‡]   Peter Boesecke [§]

Sérgio S. Funari [¶]   Ralf Schweins, Peter Lindner [‖]

Martin Westermann, Frank Steiniger [**]

May 26, 2015

Abstract

DNA-complexes with platelet-like, cationically modified lipid nanoparticles (cLNPs) are studied with regard to the formation of nanocomposite structures with a sandwich-like arrangement of the DNA and platelets.

For this purpose suspensions of platelet-like triglyceride nanocrystals, stabilized by a mixture of two nonionic (lecithin plus polysorbate 80 or poloxamer 188) and one cationic stabilizer dimethyldioctadecylammonium (DODAB), are used. The structure of the platelets in the native suspensions and their DNA-complexes, ranging from the sub-nano to the micron scale, is investigated with small- and

---

[*]Professur für Nanomaterialcharakterisierung (Streumethoden), Friedrich–Alexander–Universität Erlangen–Nürnberg, Staudtstr. 3, 91058 Erlangen, Germany, E-mail: Tobias.Unruh@fau.de

[†]German Engineering Materials Science Centre (GEMS) at Heinz Maier-Leibnitz Zentrum (MLZ), Helmholtz-Zentrum Geesthacht GmbH, Lichtenbergstr. 1, 85748 Garching, Germany

[‡]Forschungs-Neutronenquelle Heinz Maier-Leibnitz (FRM II), Lichtenbergstr. 1, 85747 Garching, Germany

[§]European Synchrotron Radiation Facility (ESRF), 71 Avenue des Martyrs, CS40220, 38042 Grenoble CEDEX 9, France

[¶]HASYLAB at DESY, Notkestr. 85, 22607 Hamburg, Germany

[‖]DS / LSS, Institut Laue-Langevin (ILL), 71 Avenue des Martyrs, CS20156, 38042 Grenoble CEDEX 9, France

[**]Center for Electron Microscopy of the Jena University Hospital, Ziegelmühlenweg 1, 07743 Jena, Germany

1

wide-angle scattering (SAXS, SANS, WAXS), calorimetry, photon correlation spectroscopy, transmission electron microscopy and computer simulations.

The appearance of strong, lamellarly ordered peaks in the SAXS patterns of the DNA-complexes suggests a stacked arrangement of the nanocrystals, with the DNA being partially condensed between the platelets. This finding is supported with computer simulated small-angle scattering patterns of nanocrystal stacks, which can reproduce the measured small-angle scattering patterns on an absolute scale.

The influence of the choice of the nonionic stabilizers and the amount of the cationic stabilizer DODAB on the structure of the native suspensions and the inner structure of their DNA-complexes is studied, too. Using high amounts of DODAB, lecithins with saturated acyl chains and polysorbate 80 instead of poloxamer 188 produces thinner nanocrystals, and thus decreases their repeat distances in the nanocomposites. Such nanocomposites could be of interest as DNA carriers, where the triglyceride platelets protect the sandwiched DNA from degradation.

Abbrevations

Materials:

CTAB   Cetyltrimethylammonium bromide

CPYC   Cetylpyridinium chloride

cLNP   Cationic lipid nanoparticles

DMPC   Dimyristoylphosphocholine

DNA   Deoxyribonucleic acid from herring testes

DODAB   Dimethyldioctadecylammonium bromide

DOPC   Dioleoylphosphocholine

DOPE   Dioleoylphosphoethanolamine

DOTAP   Dioleoyltrimethylammonium propane
           chloride

EQ1   N,N-Di-(β-stearoylethyl)-N,N-dimethyl-
           ammonium chloride (Esterquat 1)

2

μDSC	Micro-differential scanning calorimetry
MMM	Trimyristin
MSCS	Macroscopic scattering cross section ($d\Sigma/d\Omega$)
PCS	Photon correlation spectroscopy
PEG	Polyethylene glycol
PLX	Poloxamer 188 (Pluronic®F-68)
PPG	Polypropylene glycol
PPP	Tripalmitin
SAXS	Small-angle X-ray scattering
SANS	Small-angle neutron scattering
SP	Sorbitane trioleate (Span®85)
TEM	Transmission electron microscopy
TW	Polysorbate 80 (Tween®80)
WAXS	Wide-angle X-ray scattering
XNPPSA	X-ray and neutron powder pattern simulation analysis

1   Introduction

Solid lipid nanoparticles (LNP) have been studied as potential drug delivery systems
for more than 20 years.[1,2] They allow the administration of poorly water soluble drugs
and can prolong their circulation time in the body.

In the context of gene therapy, cationic LNP (cLNP) were introduced as potential
non-viral carriers for macromolecules like DNA about 15 years ago.[3,4] Viral vectors
are associated with potential safety concerns. Furthermore, in contrast to non-viral
vectors, the size of the transported macromolecules is rather limited.[4]

cLNP possess several advantages with respect to other non-viral vectors like
cationic emulsions,[5] cationic liposomes and cationic polymeric nanoparticles.[6] LNP
can be produced on a large scale with physiologically well tolerated ingredients with-
out using organic solvents.[4] However, as for other non-viral vectors, the cationic stabi-

3

lizers in the cLNP can increase their cytotoxicity considerably. LNP formulations can be steam sterilized[4] and allow drug targeting. For the latter, specific ligands grafted at the surface of the LNP promote the docking of the LNPs at the matching receptors of the target cells.[3,7] The DNA binding and in-vitro transfection efficiency for cetyl palmitate cLNP, stabilized by TW, SP and DOTAP, and liposomes prepared from the same stabilizers, were found to be very similar.[8]

In previous studies Compritol®ATO 888 (a mixture of mono-, di- and triglyerides of mainly behenic fatty acids),[3,7,9–11] Precirol®ATO 5 (glycerol distearate),[12] cetyl palmitate[8,9] or fatty acids like oleic and stearic acid were used as matrix lipids. Nonionic stabilizers like TW(+SP) and PLX and different cationic co-stabilizers like CPYC,[3,9] CTAB,[9] EQ1,[3,9] DODAB[9–11] and DOTAP[8,9,12] were used to stabilize the cLNP and to equip them with a positive charge.

The choice of the matrix lipid and, in particular, the cationic lipid can have a significant effect on the DNA immobilization, cytotoxicity and transfection of the cLNP.[9] The in-vitro cytotoxicity is often high for single-tailed cationic stabilizers like CPYC and CTAB and is reduced for double-tailed lipids like EQ1, DOTAP and DODAB.[9] Novel cationic lipids with a sophisticated design of their chains, head groups and linkers[13] like ether functionalized Gemini pyridinium amphiphiles,[14] cationic phosphatidylcholines,[15] and even single-tailed molecules like 6-lauroxyhexyl lysinate,[16] may further help to reduce the cytotoxicity of cLNP.

Further structures were proposed as non-viral vectors: Liposomes, consisting of a mixture of the cationic lipid DOTAP and a zwitterionic phospholipid (DOPE or DOPC), undergo a topological transition to liquid crystalline condensed globules with a smectic order upon addition of DNA. In these complexes the DNA chains form a 1D ordered array between the 2D membranes.[17] Similar nanocomposite structures were found in DNA-complexes with smectite clays such as montmorillonite. Thereby, X-ray diffraction indicated an intercalation of DNA between the clay nanosheets.[18]

So far, for cLNP suspensions only DNA-complexes with a few round cLNPs, prepared from Compritol®ATO 888, PLX and DODAB, were reported.[10]

Here we study sandwich-like nanocomposites of platelet-like cLNP and DNA

4

which could protect the intercalated DNA from degradation. For this purpose we considered lecithin stabilized triglyceride suspensions which are known to consist of platelet-like LNPs.[2,19,20] Addition of the cationic stabilizer DODAB imparts them with a positive charge. It is studied how the composition of the cLNPs (different amounts of the cationic and nonionic stabilizers) and the amount of added DNA (charge ratio) affects the microscopic- and nanostructure of the cLNP-DNA complexes.

2 Materials and methods

2.1 Materials
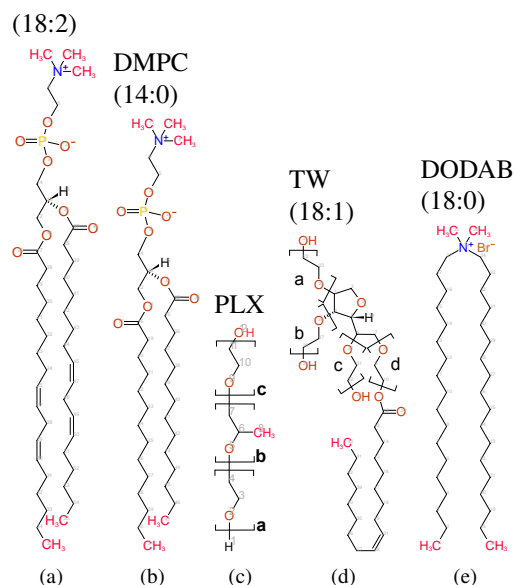
Figure 1: Molecular structures of the stabilizers used in this study, values in brackets denote the length and degree of unsaturation for the lipophilic acyl chains. For PLX it holds $a = c = 80$ and $b = 27$, for TW $a + b + c + d = 20$.

Tripalmitin (PPP, Dynasan®116, 95% purity for the fatty acid fraction) was kindly provided from Sasol GmbH, Witten, Germany. S100 was donated by Lipoid AG, Ludwigshafen, Germany. S100 is a purified soybean lecithin (>94% phosphatidylcholine). Its fatty acid composition consists predominantly of linolenic acid (18:2, 59-70%, as an example 1,2-dilinoleoyl-sn-glycero-3-phosphocholine is visualized in Fig. 1(a)), oleic

Table I: Chemical composition of the native PPP suspensions. x denotes the concentration of the cationic stabilizer.

sample	composition
PLX-x	10% PPP, 3.0% S100, 4.5% PLX, x% DODAB
TW-x	10% PPP, 2.4% S100, 6.0% TW, x% DODAB

acid (18:1, 11-15%) and palmitic acid (16:0, 12-17%). Dimyristoylphosphocholine (DMPC, 98%, Fig. 1(b)) was purchased from Lipoid AG. The PEG-PPG block copolymer poloxamer 188 (PLX, Fig. 1(c)), polysorbate 80 (TW, Fig. 1(d)), dimethyldioctadecylammonium bromide (DODAB, 98%, Fig. 1(e)) and freeze-dried DNA from herring testes (sodium salt, type XIV) were purchased from Sigma-Aldrich Chemie GmbH, Taufkirchen, Germany. All chemicals were used without further purification. Purified and filtered (cut off size 220 nm) water with an electrical resistance of 18.2 MΩ·cm or D_2O (isotopic purity 99.9% atom D, Euriso-Top GmbH, Saarbrücken, Germany) was used. In the following all concentrations regarding the composition of the cLNP suspensions are given in %wt for an equivalent fully protiated (i.e. without any deuteration) suspension.

2.2 Sample preparation and notations

2.2.1 Preparation of the native PPP suspensions

PPP suspensions stabilized by a mixture of a lecithin (S100 or DMPC), DODAB and either PLX or TW were prepared. The concentration of the cationic stabilizer DODAB was varied. The prepared native PPP suspensions are labelled as PLX-x or TW-x, where x denotes the concentration of DODAB (*cf.* Table I for the sample composition).

The native PPP suspensions were prepared by high-pressure melt homogenization. PPP (melting point 66 °C), the lecithin (S100 or DMPC) and DODAB were heated up to 80 °C until a melt was obtained. PLX or TW were dissolved in H_2O (or D_2O) and heated to the same temperature. D_2O was used for some suspensions since they were measured with small-angle neutron scattering. The hot mixture was pre-dispersed for 3 minutes with an Ultra-Turrax T25 Basic disperser (IKA-Werke GmbH & Co. KG, Staufen, Germany) at a speed of 22.000 rpm. About 40 ml of the hot pre-emulsions

6

were passed to a preheated (70 °C) APV-2000 high-pressure melt homogenizer (APV Deutschland GmbH, Unna, Germany) and homogenized for four minutes with gradually increasing pressures between 1 and 1.5 kbar. The nanoemulsions were allowed to cool down to room temperature and finally stored in crimped glass vials at 6 °C.

Throughout the graphs in the article a uniform color scheme is used for the native PPP suspensions: PLX-0.4 (**black**), PLX-1.2 (**red**), PLX-2.0 (**green**), TW-0.4 (**blue**), TW-0.8 (**orange**), TW-1.6 (**magenta**) and TW-2.5 (**cyan**).

2.2.2 Preparation of the cLNP-DNA complexes

DNA complexes were prepared from the native suspensions. They differ in final PPP concentration (1 and 3%, for PLX-0.4 also 7%) and the amount of added DNA. The latter is expressed by the charge ratio ξ between the amount of cationic DODAB molecules (n_{DODAB}, one positive charge per molecule) and the amount of anionic nucleotides (n_{nc}, one negative charge per nucleotide) of the DNA. Thus, ξ is given by

$$\xi = \frac{n_{DODAB}}{n_{nc}} = \frac{m_{DODAB}}{m_{DNA}} \cdot \frac{M_{nc}}{M_{DODAB}} \tag{1}$$

m_{DODAB} and m_{DNA} denote the mass of DODAB and DNA in the complexes, respectively. For the (average) molar mass of one nucleotide M_{nc} we use 331 g/mol, M_{DODAB} is 630 g/mol. $\xi = \infty$ refers to samples without DNA. For samples with $\xi = 1$ the isoelectric point is reached.

The cLNP-DNA complexes were prepared in the following way: For each native suspension an appropriate DNA stock solution was prepared from the DNA and H_2O (or D_2O). Appropriate amounts of the DNA stock solution and further H_2O (or D_2O) were transfered into a 1.7 ml reaction tube to meet the desired final triglyceride concentration and charge ratio. An appropriate amount (typically 100 or 200 mg) of the native suspension was added into the lid of the reaction tube. After the lid was closed, the reaction tube was immediately vortexed for 30 s.

The charge ratios ξ of the cLNP-DNA complexes (irrespective of which native suspension they were prepared from) are colour-coded in the graphs as: ∞ (**black**), 10

(**red**), 3 (**green**), 2 (**blue**), 1 (**orange**), 0.7 (**magenta**), 0.5 (**cyan**) and 0.3 (**brown**).

2.3 Photon correlation spectroscopy (PCS)

Photon correlation spectra were measured using a photon correlation spectrometer (Brookhaven Instruments Corporation, Holtsville, NY, USA) consisting of a Mini-L 30 compact diode laser (30 mW, 637 nm) and a BI-200 SM goniometer carrying the photo multiplier tube at a scattering angle of $90°$. Without further filtration, a few droplets of the sample were diluted with appropriate amounts of filtered (cut off size 220 nm), purified water in a glass cuvette until a count rate of about 50 - 100 kcps was obtained. The samples were measured for 2 min at room temperature (22 °C). The z-averaged hydrodynamic diameter d_{PCS} and polydispersity index PdI were determined by applying the cumulant method to the measured correlation function.

2.4 Micro differential scanning calorimetry (μDSC)

A Micro DSC III (Setaram, Caluire-et-Cuire, France) was used for the micro-calorimetric heating and cooling scans. About 200 mg of the samples were filled in the sample holders, heated from 5 °C to 70 °C and subsequently cooled back to 5 °C at a scan rates of 0.1 K/min. The reference cell was filled with the same amount of water. The enthalpies of fusion and crystallization were determined by an integration of the heating and cooling curves, respectively, within a region of interest. For suspensions prepared with D_2O the enthalpies were corrected for the difference in weight density between H_2O and D_2O.

2.5 Cryo- and freeze-fracture transmission electron microscopy (TEM)

The cryo- and freeze-fracture transmission electron micrographs were recorded as described elsewhere.[21–24]

8

2.6 Small- and wide-angle X-ray scattering (SAXS, WAXS)

The SAXS and WAXS patterns for the native PPP suspensions and the corresponding cLNP-DNA complexes were recorded at the high brilliance beamline ID02 at ESRF in Grenoble. Samples were measured for 0.1 s at 1.6 m and 6 m sample-detector distance with a wavelength of $\lambda = 1 \text{ Å}$. The samples were contained in a home-made sample holder with five silver cells (diameters 5 mm, sample thicknesses 1 mm). The cells are embedded in a copper block whose temperature was set to 25 °C with an external water bath. The cells were covered on both sides by mica windows (20 μm thickness). Using the sample transmission and thickness and a 1 mm water sample as a primary standard, the scattered intensities were put on an absolute scale (in units of (1/cm/sr)). The 2D SAXS patterns were azimuthally averaged and the scattering pattern of water subtracted therefrom. The scattering angles 2θ were converted to an s-scale via $s = Q/(2\pi) = (2/\lambda)\sin(2\theta/2)$.

Further SAXS patterns were measured at 25 °C with a wavelength of 1.5 Å at the former A2 beamline at HASYLAB (DESY, Hamburg, Germany), using the same sample holder. The SAXS patterns were collected with a 2D MarCCD165 detector. The sample-detector distance of 2738 mm and the beam center were calibrated using a rat tail collagen standard. A scattering pattern of water was subtracted. A WAXS pattern of β-PPP powder was recorded for 60 s at the A2 beamline with a line detector at a sample-detector distance of 135 mm.

2.7 Small-angle neutron scattering (SANS)

SANS patterns were measured at the D11 beamline at Institut Laue Langevin (ILL), Grenoble. The samples were contained in Starna 21/Q/0.5 Spectrosil quartz cuvettes with 0.5 mm sample thickness (Starna GmbH, Pfungstadt, Germany), placed in a copper-made multi-position sample holder, provided at the beamline. The temperature was set with an external water bath to 25 °C. The velocity selector provided a wavelength of $\lambda = 6 \text{ Å}$ with a wavelength spread of $\Delta\lambda/\lambda = 9\%$. The samples were measured at three different instrumental setups (sample-detector distance/collimation

9

length), namely 1.2/5.5, 8/13.5 and 39/40.5 m, to access an $s = Q/(2\pi)$-range of

$0.0025\ldots0.8\,nm^{-1}$. The 2D raw data were corrected for dark current (measured by

placing a boron carbide slab at the sample position), scattering of the empty sample

holder, transmission, detector sensitivity, and were put on an absolute scale (1/cm/sr),

using a 1 mm thick H_2O sample. Finally, the corrected 2D images were azimuthally

averaged. Measurements of the aqueous backgrounds were not subtracted, since water

(D_2O) scatters approximatively flat in the small-angle range. Later, this can be mod-

elled with an additional constant in the fits.

2.8 X-ray and neutron powder pattern simulation analysis (XNPPSA)

The XNPPSA method allows the computation of SAXS and SANS patterns within the

kinematic scattering theory for different structures formed by nanocrystals in a disper-

sion. Their frequencies can be determined by a simultaneous fit of a linear combination

of their macroscopic scattering cross sections (MSCSs) ($d\Sigma/d\Omega$) to the experimen-

tal data.[21–25] Structures can be for example single nanocrystals[21] and stacks of such

nanocrystals.[22] The nanocrystals can be covered by up to two shells.

The simulation method is particularly suited for the analysis of small-angle scatter-

ing patterns of nanocrystalline dispersions which exhibit broad Bragg peaks.

For dilute triglyceride nanosuspensions, it was demonstrated that the broadened

001 Bragg peak of the triglyceride nanocrystals in the SAXS and SANS patterns is of

great benefit to determine the distribution of the thicknesses of the nanocrystals with

molecular resolution. Furthermore, the structure of the stabilizer layer at the interface

between the nanocrystals and the aqueous dispersion medium was investigated.[21,22,25]

At higher concentrations, self-assembled stacks of triglyceride nanocrystals were

studied.[22–25]

Here we used the XNPPSA method:

(1) to determine the distribution of the thicknesses of the platelet-like nanocrystals
    in the native PPP suspensions, and

10

(2) to demonstrate, that the rather complicated small-angle scattering patterns of the cLNP-DNA complexes originate from stacked PPP nanocrystals.

Problem (1) was solved, using the native PPP suspensions in dilute form (3% PPP, $\xi = \infty$), to avoid self-assemblies of nanocrystals in the suspensions (typically found for PPP concentrations $\geq 4\%$ [23,26]). Therefore, only isolated platelets of different thicknesses and diameters (*cf.* Fig. 2(a)) were used as structural elements in the computer simulations.

For problem (2), platelet stacks (*cf.* Fig. 2(b)) were included as additional structural elements to model the cLNP-DNA nanocomposites.

As an example, Fig. 2(c) shows the structural model for a stack consisting of three PPP nanocrystals in the stable β-modification in detail. The stacking direction coincides with the direction of the reciprocal $\mathbf{G}_{001}$ lattice vector. Isolated platelets can be considered as a special case of a stack, consisting of only one nanocrystal. The atomic positions of the β-PPP molecules and the parameters for β-PPP's triclinic unit cell were taken from van Langevelde *et al.* [27] (top-right inset in Fig. 2(c)).

Each platelet has a parallelepipedal shape, where the two lateral lengths were subject to a Gaussian distribution with a mean of 100 nm and a variance of 20 nm. Because of the amphiphilic character of the stabilizer molecules, each nanocrystal is covered by two shells (top-bottom inset in Fig. 2(c)) with constant electron density (SAXS) and neutron scattering length density (SANS) profiles for each shell. The inner shell (is, thickness d_{is}) is dedicated for the lipophilic parts of the stabilizer molecules (fatty acid residues for S100, DODAB and TW; PPG blocks for PLX) and the outer shell (os, thickness d_{os}) for their hydrophilic parts (phosphocholine head groups for S100, dimethylammonium head group for DODAB and essentially PEG blocks for TW and PLX) and the DNA.

Since the single nanocrystals and nanocrystal stacks can assume all orientations, a powder average is carried out in the computations of their MSCSs. [21]

For problem (1), the MSCSs $(d\Sigma/d\Omega)_{sp}^{i}$ were computed for five ensembles ($i = 1, \ldots, 5$), each consisting of 400 single platelets (sp). All platelets in ensemble i share a common thickness of i unit cells β-PPP, but vary in their lateral sizes. The thickness
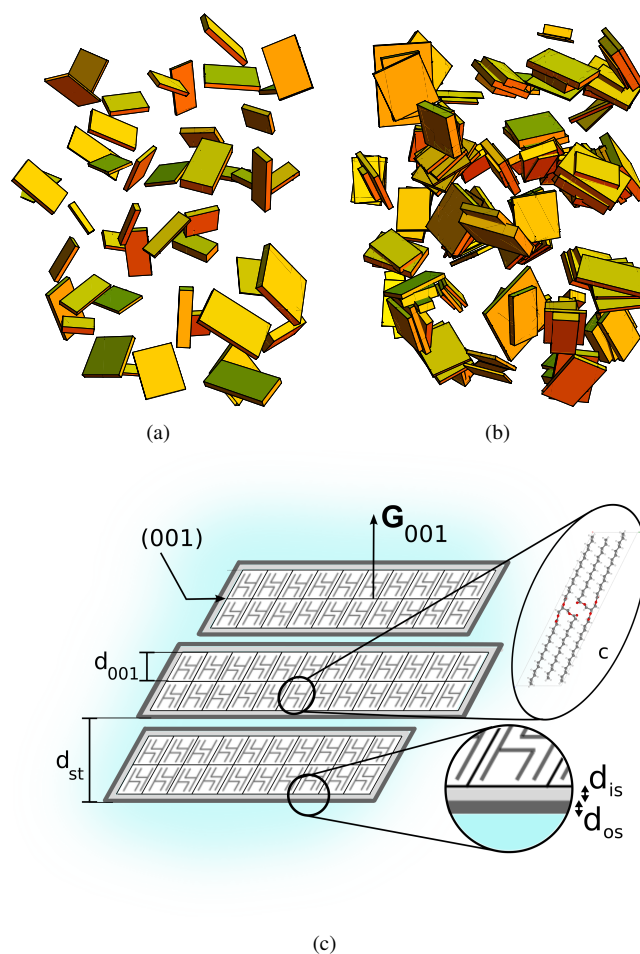
11

Figure 2: Schematic illustration of the simulation model for a suspension (a) before (only individual nanocrystals) and (b) after addition of DNA (DNA-induced stack formation of the nanocrystals in the complexes). (c) Detailed structural model for a stack of three nanocrystals. Each nanocrystal is covered by two shells, an inner (is) and outer shell (os), with thicknesses d_{is} and d_{os} (lower inset). The molecular arrangement of the PPP molecules in the triclinic unit cell for β-PPP is indicated in the upper inset.

d_{001} of one β-PPP unit cell in direction of $\mathbf{G}_{001}$ is 4.02 nm (Fig. 2(c)).[21,27]

For problem (2), the MSCSs $(d\Sigma/d\Omega)_{st}^i$ for three ensembles ($i = 2, 3, 4$) of stacks (st) are simulated. Ensemble i consists of 100 stacks with each stack consisting of i platelets. The repeat distances of the platelets in the stacks follow a Gaussian distribution with mean d_{st} (Fig. 2(c)) and variance σ_{st}.

The computer simulations were performed using the C++ program *XNDiff*. As described in more detail in the Results section, simulations with different combinations

of the shell thicknesses d_{is} and d_{os} (problems (1) and (2)) and repeat distances $d_{st} \pm \sigma_{st}$ (problem (2)) were carried out.

For problem (2), the X-ray and neutron MSCS ($d\Sigma/d\Omega$) can be expressed as a linear combination of the ensembles of isolated platelets with different thicknesses, $(d\Sigma/d\Omega)^i_{sp}$, and stacks with different numbers of platelets per stack, $(d\Sigma/d\Omega)^i_{st}$, as [22]

$$\left(\frac{d\Sigma}{d\Omega} \right) = \sum_{i=1}^{5} c_i \left(\frac{d\Sigma}{d\Omega} \right)^i_{sp} + \sum_{i=2}^{4} d_i \left(\frac{d\Sigma}{d\Omega} \right)^i_{st} + A \qquad (2)$$

The second sum for the stacks is omitted for problem (1). The constant $A > 0$ is used in the fits to match the backgrounds at higher scattering angles.

Each simulated data set was (simultaneously) fitted with the Mathematica program *BatchMultiFit* to the SAXS (and SANS) data using Eq. 2. The source code of *BatchMultiFit* and *XNDiff* are available free of charge on https://sourceforge.net/projects/xndiff/.

The fitted linear coefficients c_i in Eq. 2 can be interpreted as the volume fractions of isolated platelets with a thickness of i unit cells. Thus, the c_i provide a volume weighted distribution of the platelet thicknesses. [21] Likewise, in problem (2), the fitted d_i can be interpreted as the volume fractions of stacks, consisting of i platelets. In the fits the volume fractions c_i (and d_i) must fulfill the completeness relation

$$\sum_{i=1}^{5} c_i \left(+ \sum_{i=2}^{4} d_i \right) = 1 \qquad (3)$$

The electron densities (EDs) ρ^X_{is}, ρ^X_{os} and ρ^X_{dm}, and the neutron scattering length densities (NSLDs) ρ^n_{is} and ρ^n_{os} for the inner and outer shell and the dispersion medium (dm) are included in the mathematical expressions for $(d\Sigma/d\Omega)^i_{sp}$ and $(d\Sigma/d\Omega)^i_{st}$. Apart the c_i (and d_i) from Eq. 2, these EDs and NSLDs can be fitted, too. [21,22] ρ^n_{dm} was fixed in the fits to the NSLD of D_2O. The EDs and NSLDs in both shells were allowed to range between 270 and 540 nm^{-3} and $-0.5 \cdot 10^{-6}$ and $6.3 \cdot 10^{-6}$ Å^{-2}, respectively (ranges estimated in part A of the Supplementary Material).

Uncertainties / error bars (mean and variance) for the fit parameters were calculated.

13

For this purpose, the fitted values of a class of good fits (which deviated only slightly in quality from the best fitted data set) from further simulated data sets were used. [22,23]

The completeness relation in Eq. 3 was relaxed in the fits, such that the sum may vary within 20% bounds around 1. In the simultaneous SAXS and SANS fits a scaling factor χ ($0.8 \leq \chi \leq 1.2$) was permitted for the SAXS curve. The simulated SANS patterns were smeared prior to the fitting, using the wavelength spread $\Delta\lambda/\lambda = 0.09$. [21]

3   Results and Discussion

3.1   Preliminary investigations

In a first attempt, cationically modified versions of S100-stabilized triglyceride LNP suspensions were studied. Suspensions with different cationic, single-tailed (CPYC, C_6TAB, C_{10}TAB, C_{12}TAB, C_{16}TAB) or double-tailed (DODAB, DOTAP) co-stabilizers were prepared and evaluated with regard to their stability and ability to form sandwich-like nanocomposites with the DNA. As it is described in detail in part B of the Supplementary Material, some formulations with single-tailed co-stabilizers could produce stable cLNP suspensions. However, none of them was able to produce cLNP-DNA complexes with a stacked arrangement of the platelets and DNA. The native suspensions with double-chain costabilizers gelled upon crystallization.

In a next step the triglyceride cLNP formulations, introduced in Sec. 2.2, were tested. They were prepared from tripalmitin (PPP), the lecithin blend S100, the cationic co-stabilizer DODAB and, now, additionally another nonionic costabilizer: PLX or TW (composition and notation follows Table I). Addition of PLX / TW produces PEGylated cLNP, which do not gel anymore upon crystallization.

In the following the results of the structural characterization of the native PLX-x and TW-x suspensions and their DNA-complexes are presented.

Table II: z-averaged hydrodynamic particle diameters (d_{PCS}) and polydispersity indices (PdI) for the native suspensions. The enthalpies of fusion (ΔH_{fus}) and crystallization (ΔH_{cry}), derived from the μDSC heating and cooling runs in Figs. 4, are listed, too. ΔH_{fus}^* denotes the enthalpy of fusion associated with the melting of particles with the unknown PPP modification.

sample	PCS		μDSC			
	d_{PCS}	PdI	ΔH_{fus}	ΔH_{fus}^*	$\frac{\Delta H_{fus}^*}{\Delta H_{fus}}$	ΔH_{cry}
	[nm]	[-]	[J/g]	[J/g]	[%]	[J/g]
PLX-0.4	149.3	0.25	17.7	1.7	9.4	-16.8
PLX-1.2	120.3	0.24	17.5	5.0	28.6	-17.4
PLX-2.0	131.2	0.26	17.6	6.4	36.6	-18.0
TW-0.4	102.2	0.26	17.9	3.9	22.0	-17.8
TW-0.8	113.9	0.26	18.0	6.7	37.4	-18.1
TW-1.6	98.7	0.28	17.7	13.1	74.0	-17.4
TW-2.5	87.9	0.32	18.2	11.7	64.3	-18.6

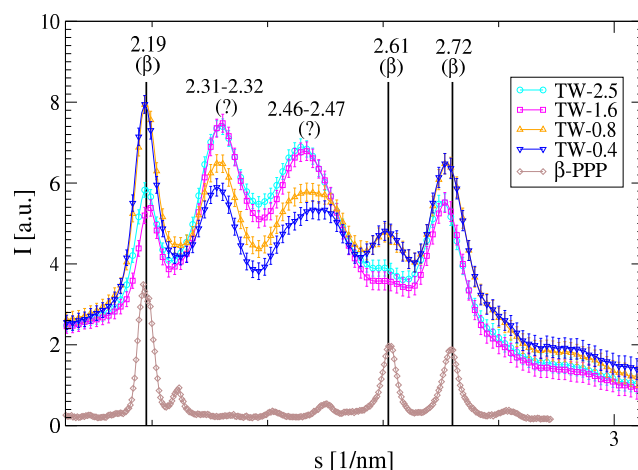## 3.2 Native cLNP suspensions

3.2.1 PCS measurements

The measured hydrodynamic diameters d_{PCS} (which can be regarded as a rough estimate for the platelet diameters) and polydispersity indices PdI of the native suspensions are listed in Table II. For the PLX-x series the d_{PCS} values range between 120 and 150 nm. PdI values ≥ 0.24 indicate broad size distributions. For the TW-x series, significantly lower d_{PCS} diameters between 88 and 114 nm are obtained. Rising the amount of DODAB from 0.4 to 2.5% decreases the particle size, but broadens the size distribution up to a PdI value of 0.32.

3.2.2 WAXS measurements

The WAXS patterns of the native PPP suspensions are visualized in Fig. 3. All suspensions of the PLX-x series exhibit the three strongest, characteristic reflections of the β-modification at $s = 2.19$, 2.61 and 2.72 nm^{-1}. However, three additional reflections at 2.32, 2.45 and 2.52 nm^{-1} exist for PLX-0.4. These reflections do not fit any of the known characteristic reflections of the stable β- and the thermodynamically metastable α- (one characteristic broad reflection at 2.41 nm^{-1}) and β′-modifications (2.38 and 2.63 nm^{-1}).[28]
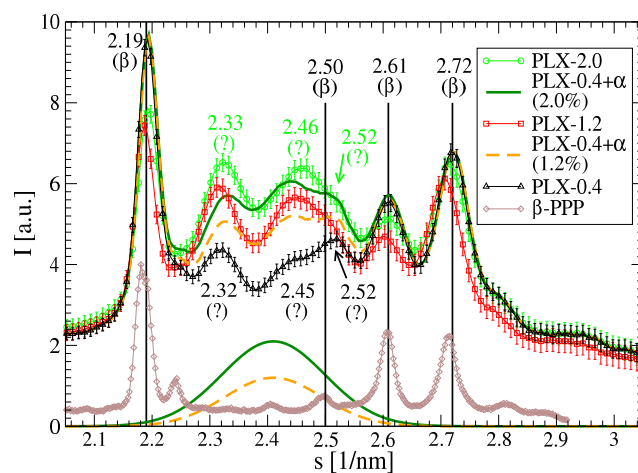
(a) Native PPP PLX-x suspensions

(b) Native PPP TW-x suspensions

Figure 3: WAXS patterns measured at the ID02 beamline for the native PPP suspensions stabilized with (a) PLX and (b) TW and different amounts of DODAB. The WAXS pattern of β-PPP powder (A2 beamline) is shown (brown diamonds), too. The positions of four strong reflections of β-PPP (2.19, 2.50, 2.61 and $2.72\,\text{nm}^{-1}$) are marked by vertical black solid lines. Additional reflections at 2.32 - 2.33, 2.45 - 2.46 and $2.52\,\text{nm}^{-1}$, observed for the dispersions, cannot be attributed to any known PPP modifications and are labelled by a question mark (?).

The first two unknown reflections appear at similar positions as reported by Bunjes *et al.* for tyloxapol stabilized MMM and PPP suspensions (2.27 and $2.44\,\text{nm}^{-1}$).[29] There it was demonstrated, that they belong to very fine platelets (diameters of only about 25 - 30 nm and small thicknesses) with an unknown triglyceride modification. In

DSC heating scans they caused pre-transitions in a temperature range between 30 °C and 38 °C for MMM suspensions (about 10 °C higher for PPP), prior to the melting of the platelets in the β-modification. [29]

If the amount of DODAB rises (PLX-1.2, PLX-2.0), the first two unknown reflections shift slightly by about $0.01\,\text{nm}^{-1}$ to higher s values. Their intensities increase considerably, while the β-related peaks decrease. Thus, higher concentrations of DODAB promote the crystallization of the unknown PPP modification.

From the WAXS patterns alone, the presence of the α-modification cannot be completely ruled out. Triglyceride LNP, crystallized into the metastable α-modification, exhibit a broad reflection at $2.41\,\text{nm}^{-1}$ in WAXS patterns. [20] For test purposes, appropriate contributions from the α-modification, modelled with a Gaussian peak profile centered at $2.41\,\text{nm}^{-1}$, were added to the WAXS pattern of PLX-0.4 to match the WAXS patterns of PLX-1.2 (dashed orange curves labelled as PLX-0.4+α (1.2%) in Fig. 3(a)) and PLX-2.0 (solid green curves labelled as PLX-0.4+α (2.0%)). Although this does not fully reproduce the diffraction patterns of PLX-1.2 and PLX-2.0, a certain amount of particles in the α-modification could be present in the dispersions. Later, in section 3.3.2, TEM micrographs can rule out the α-modification more clearly.

For the suspensions of the TW-x series similar results are obtained (Fig. 3(b)). Two unknown peaks at 2.32 and $2.46\,\text{nm}^{-1}$ considerably rise in intensity with increasing DODAB concentration, while the fraction of β-PPP decreases. Not only DODAB, but also TW seems to promote the crystallization of the unknown modification. Their reflections are for TW-0.4 already considerably larger than for PLX-0.4.

3.2.3 μDSC measurements

The micro-calorimetric heating and cooling runs are visualized for the native suspensions of the PLX-x and TW-x series in Figs. 4(a) and Fig. 4(b), respectively. The heating runs can be divided into two sections. Based on the findings from Bunjes *et al.* and the WAXS patterns, the first section between 35 and 46 °C (marked by the dashed boxes with the question mark in Figs. 4(a) and 4(b)) can be assigned to the melting events of the unknown PPP modification and possible traces of the α-modification.

The second section from 46 to 66 °C can be attributed to the melting of platelets in the β-modification (marked by the dashed boxes with the label β). Each peak in this range corresponds to the melting of platelets with a specific thickness. [29,30] With increasing DODAB concentration, the melting contributions in the first section rise considerably at the expense of the second section. The total enthalpies of fusion and crystallization, ΔH_{fus} and ΔH_{cry}, obtained by an integration of all peaks between 10 and 66 °C are listed in Table II. The values for ΔH_{fus} do not change considerably with rising DODAB concentration, indicating that the enthalpy of fusion for the unknown modification is quite similar to the 188 J/g of bulk β-PPP. [31]

Table II lists also the enthalpies of fusion ΔH_{fus}^{*} of the particles crystallized in the unknown modification (pre-transitions integrated in the range between 35 and 46 °C, dashed box with question mark in Figs. 4(a) and 4(b)). The relative fraction $\Delta H_{fus}^{*}/\Delta H_{fus}$ is used to estimate the amount of the unknown modification. For the suspensions with 0.4% DODAB the β-modification dominates clearly. However, the fraction of the unknown modification rises up to one third for PLX-2.0 and more than two-thirds for TW-1.6 and TW-2.5. Thus, in good agreement with the WAXS measurements, the micro-calorimetric data suggest that DODAB and TW promote a crystallization of the unknown modification at the expense of the β-modification.

For platelets in the β-modification, it can be anticipated that they are on average thinner in the TW-x series than in the PLX-x series. This is because the distribution of their melting events is significantly shifted to lower temperatures. For the TW-x series nearly all platelets melted below temperatures of about 56 °C, whereas for the PLX-x series this was found not until about 60 °C.

The cooling runs in Fig. 4 exhibit a main crystallization peak. For suspensions with higher DODAB concentrations (PLX-1.2, PLX-2.0, TW-1-6 and TW-2.5), this peak is preceded at higher temperatures by one or more pre-transitions. The temperature of the main crystallization event shifts with increasing DODAB concentration to higher temperatures: from 22.8 °C (PLX-0.4) to 25.0 °C (PLX-2.0) and from 21.4 °C (TW-0.4) to about 24.3 °C (TW-1.6 and TW-2.5). Similarly, the onset of the first pre-transition extends to higher temperatures with increasing DODAB concentration. While for TW-

18
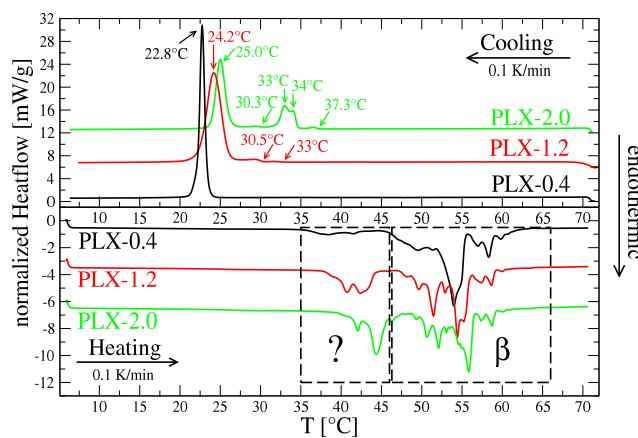
(a) Native PPP PLX-x suspensions
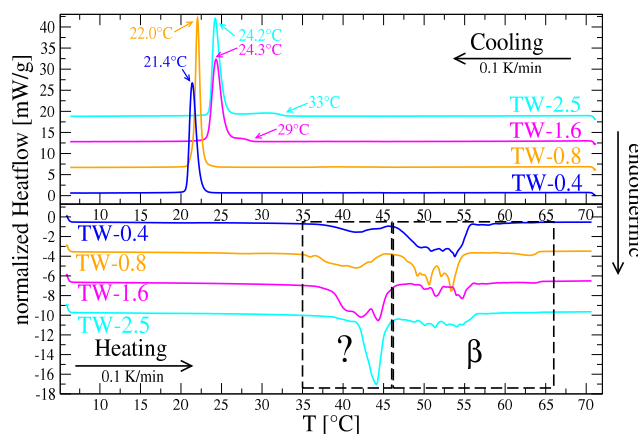
(b) Native PPP TW-x suspensions

Figure 4: μDSC heating and cooling runs for the native PPP suspensions of the (a) PLX-x and (b) TW-x series. The heating and cooling curves were shifted vertically in steps of 6 and -3 mW/g, respectively, with respect to the curves for PLX-0.4 and TW-0.4. Boxes, framed with dashed lines, mark the temperature ranges associated with the melting of platelets in the unknown (?) and β-PPP modification.

1.6 and TW-2.5 only one pre-transition exists, for PLX-1.2 and PLX-2.0 up to four pre-transitions are observed.

In a previous study on suspensions of triglyceride LNP, stabilized by lecithins of different lengths of their saturated acyl chains, it was found that the temperatures of such pre-transitions in the cooling runs correlate roughly with the phase transition temperatures of the lecithins. The pre-transitions in the cooling curves were attributed to a solidification of the saturated acyl chains of the lecithin molecules, stabilizing the

emulsion droplets prior to the crystallization of the super-cooled emulsion droplets it-self.[32]

The liquid crystalline to gel phase transition temperature for unilamellar DODAB vesicles in aqueous suspensions is about 40 °C.[33] Thus, the pre-transitions in the cooling runs might be induced by a solidification of DODAB's saturated 18:0 acyl chains in the stabilizer layer of the emulsion droplets. A higher concentration of solidified DODAB molecules in the stabilizer layer might also explain the higher temperatures of the main crystallization peak. The crystallized DODAB molecules could promote the crystallization of the triglyceride core by a template effect.

3.2.4 SAXS measurements

The SAXS patterns of the native suspensions are shown in Fig. 5(a) (in the following, error bars are smaller than the thickness of the line or symbols for the SAXS and SANS patterns). In the s-range between 0.12 and 0.34 nm^{-1} the SAXS patterns feature a broadened 001 Bragg reflection of the PPP nanocrystals.[27] Since the platelets possess a thickness of only a few molecular layers of PPP and their large faces coincide with the (001) lattice planes (the reciprocal lattice vector $\mathbf{G}_{001}$ is parallel to the platelet directors, *cf.* Fig. 2(c)), the 001 Bragg peak is strongly broadened. All SAXS patterns exhibit another peak between $s = 0.025$ nm^{-1} and 0.033 nm^{-1} which can be attributed to self-assembled platelet stacks with typical mean repeat distances d_{st} of the platelets between 30 and 40 nm.[26,34] For PLX-1.2 and PLX-2.0, even higher orders can be observed, indicating larger or better ordered stacks. The stack formation in the native suspensions (without DNA) is a concentration dependent process, upon dilution the stacks disintegrate.[26]

For all suspensions, the position s_{001} of the 001 Bragg peak is shifted to smaller s-values compared to bulk β-PPP ($s_{001} = 0.249$ nm^{-1}). Besides the broadening, the shift can be attributed to the small thicknesses of the platelets, too.[20]

The positions s_{001} and widths (measured by the variance σ_{001}) of the 001 Bragg peaks, determined by a fit with a Gaussian peak profile: $A \cdot \exp\left[-(s-s_{001})^2/(2\sigma_{001}^2)\right] + C$ (A and C constants), are listed in Table SIII in the
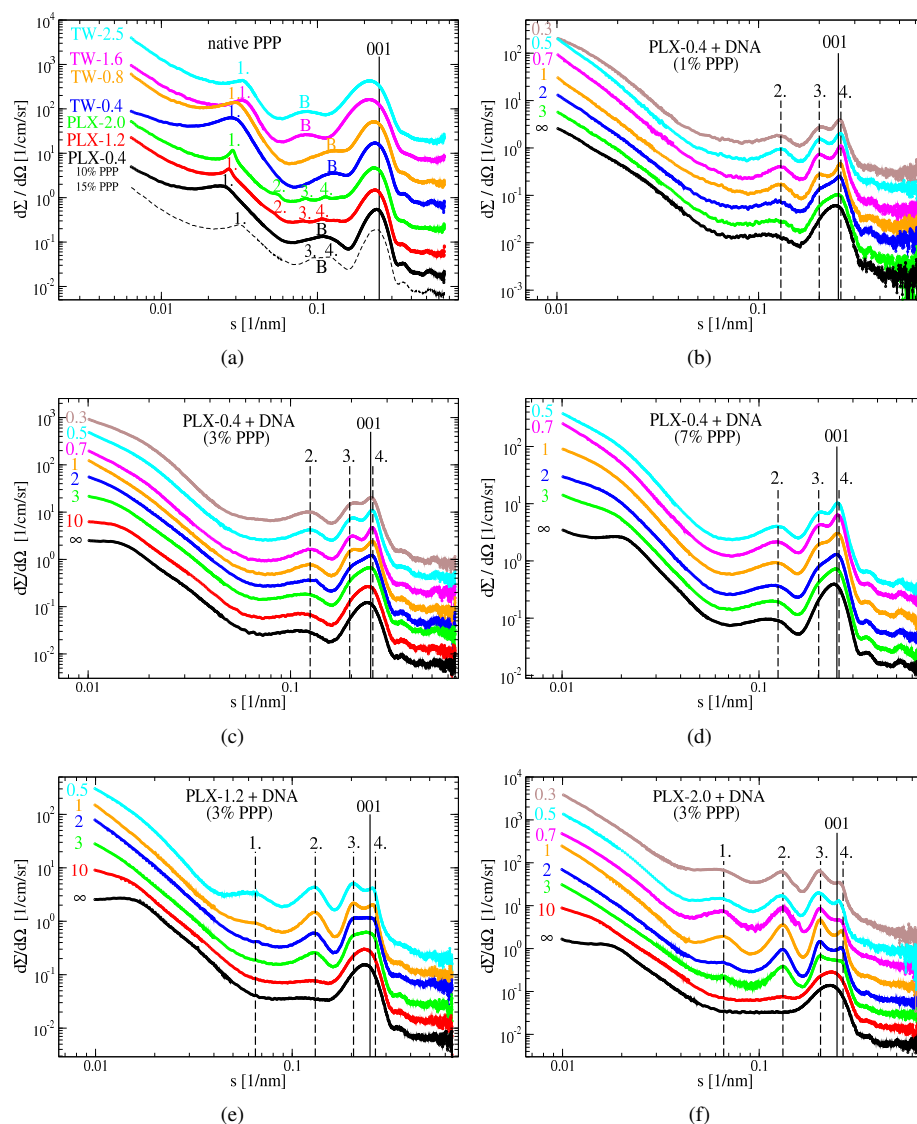
Figure 5: (a) SAXS patterns (ID02 beamline) for the native suspensions. The scattering pattern of a PLX-0.4 suspension with 15% PPP is plotted, too (black dashed line). The interference maxima of the self-assembled stacks are labelled up to the fourth order by numbers. (b-f) SAXS patterns of cLNP-DNA complexes with charge ratios in the range ∞ (no DNA) to 0.3 prepared from the PLX-x series: (b) PLX-0.4 (1% PPP), (c) PLX-0.4 (3% PPP), (d) PLX-0.4 (7% PPP), (e) PLX-1.2 (3% PPP) and (f) PLX-2.0 (3% PPP). For clarity, the SAXS patterns were shifted vertically, starting from the solid black curve at the bottom ($\xi = \infty$). The position of the 001 Bragg reflection for bulk β-PPP and the first four orders of the stack-related interferences are marked by vertical lines.

21

Supplementary Material. The shifts and the widths of the 001 Bragg peak rise with increasing DODAB concentration and when using TW instead of PLX. They are particularly strong for the suspensions TW-1.6 and TW-2.5. Such a strong broadening of the 001 Bragg peak was reported by Bunjes *et al.* for suspensions containing many thin platelets of the unknown triglyceride modification.[29] Thus, in accordance with the WAXS and μDSC measurements, the strong peak broadening can be attributed to the large number of platelets crystallized in the unknown PPP-modification, which are significantly thinner than those of the β-modification.

However, the broadening and shift to smaller *s*-values of the 001 Bragg peak could also partially stem from an additional Bragg reflection of the unknown PPP modification, which overlaps the 001 Bragg peak of the β-PPP platelets.

Some suspensions (PLX-0.4, TW-x) also feature a broad bump (labelled with B in Fig. 5(a)) between the tail of the diffuse small-angle scattering and the 001 Bragg peak. For PLX-0.4 the position s_b is $0.109\,\text{nm}^{-1}$. s_b shifts from $0.128\,\text{nm}^{-1}$ for TW-0.4 and TW-0.8 to $0.085\,\text{nm}^{-1}$ for TW-1.6 and TW-2.5 (Table SIII).

If the PPP concentration for a PLX-0.4 suspension is increased from 10% to 15% PPP, the bump is clearly deformed (black dashed curve in Fig. 5(a)). This can be explained by an interference between the scattering causing the bump and the stack-related scattering. While the 2nd order of the stack-related interference maxima cannot be observed, the 3rd and 4th orders are clearly enhanced around the bump. Structures like vesicles and micelles cannot cause the bump, since their scattering would not interfere with the scattering of the stacked lamellae. Thus, the bump must be related to an unknown inner structure of the platelets (periodicities between $d = 7.8\,\text{nm}$ ($s = 0.128\,\text{nm}^{-1}$) and $d = 11.8\,\text{nm}$ ($s = 0.085\,\text{nm}^{-1}$)) or to their form factor (shape). The latter could be due to a larger fraction of platelets with a particular thickness. Later, in section 3.3.6, it is demonstrated with the XNPPSA method, that the presence and position of the bump is indeed related to different platelet thickness distributions in the native suspensions.

The SAXS patterns for the PLX-1.2 and PLX-2.0 suspensions do not exhibit such a bump explicitly. However, due to the relatively high strength of the 4th order with

respect to the 3rd and 2nd order, these suspensions also feature a small bump at a similar position as for PLX-0.4.

3.3 cLNP-DNA complexes

The cLNP-DNA complexes were prepared from the native suspensions with final PPP concentrations of typically 1% or 3% and charge ratios ranging from ∞ to 0.3. They were structurally characterized by PCS, TEM, µDSC, SAXS and SANS and using the XNPPSA method. The effects of using a different lecithin (DMPC instead of S100) and PPP-free cLNP suspensions as a reference were studied, too.

3.3.1 PCS measurements
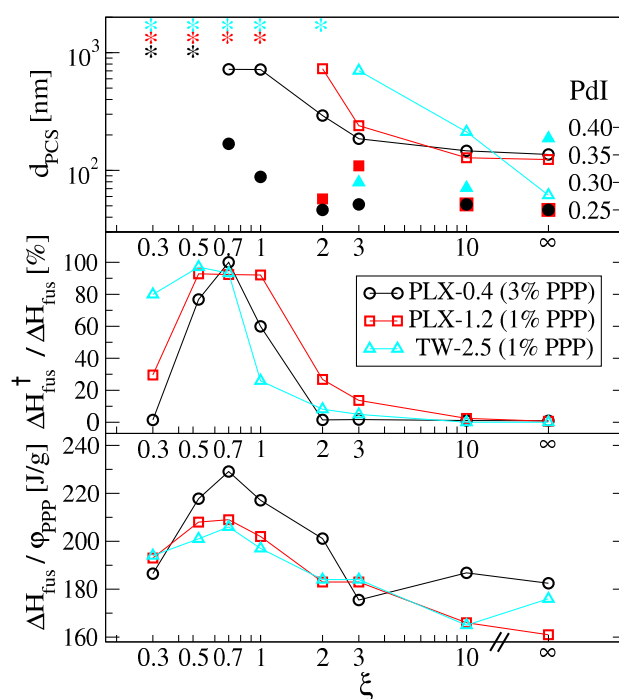
Figure 6: cLNP-DNA complexes at different charge ratios ξ prepared from PLX-0.4 (black $\bigcirc$), PLX-1.2 (red $\square$) and TW-2.5 (cyan $\triangle$): (top) PCS z-averages d_{PCS} (open symbols with solid lines) and polydispersity indices (filled symbols). Starred points (*) mark measurements with $d_{PCS} > 1\,\mu m$. (middle) Fraction of macroscopic agglomerates with respect to the total dispersed phase, derived from the µDSC data. (bottom) Enthalpy of fusion normalized by the PPP concentration φ_{PPP}. The data was taken from Tables SIV(a), SIV(b) and SIV(c).

PCS measurements were carried out for cLNP-DNA complexes prepared from the suspensions PLX-0.4, PLX-1.2 and TW-2.5. The corresponding z-averaged particle diameters d_{PCS} and PdI values are listed in Tables SIV(a), SIV(b) and SIV(c), respectively, and are plotted in the top part of Fig. 6. With decreasing charge ratio ξ, agglomeration rapidly increases. The measured d_{PCS} start close to the values of the native suspensions (*cf.* Table II) and increase rapidly to several hundred nanometers. For charge ratios ξ lower than 0.7 (PLX-0.4), 2 (PLX-1.2) and 3 (TW-2.5), d_{PCS} values in the micron range were obtained. Using standard PCS technique and data evaluation, reliable results can be provided only for particle diameters up to a few hundred nm. Larger values can be considered only as a crude approximation for the particle size.[35,36] Values $d_{PCS} > 1\,\mu$m were not considered meaningful and are marked with a $*$-sign in Tables SIV(a), SIV(b), SIV(c) and in Fig. 6. For cLNP-DNA complexes prepared from PLX-1.2, PLX-2.0, TW-1.6 and TW-2.5 and charge ratios close to 1, large agglomerates were often visible to the naked eye.

The final PPP concentration of 1% or 3% has only little influence on the size of the complexes as further tests with PLX-0.4 and PLX-1.2 revealed (data not shown). The size of the complexes is primarily determined by the DODAB concentration in the native suspension and the added amount of DNA. Higher amounts of DNA (*i.e.* smaller ξ) and DODAB increase the size of the cLNP-DNA complexes. Interestingly, for the cLNP-DNA complex prepared from PLX-0.4 with a charge ratio 0.3, a decrease in the d_{PCS} value was found with respect to $\xi = 0.5$. The size was still larger than 1 micron, but micro-calorimetric data, presented later, supports the finding that the fraction of large cLNP-DNA complexes decreases for sufficiently low charge ratios and native suspensions with low DODAB concentrations.

3.3.2 TEM micrographs

Freeze-fracture and cryo TEM micrographs were taken for a selected number of cLNP-DNA complexes with d_{PCS} values below 1 micron. Fig. 7(a) shows a freeze-fracture TEM micrograph of complexes prepared from PLX-0.4 ($\xi = 1$, 3% PPP). Besides single platelets, several agglomerates with sizes of a few hundred nanometers can be

24

found. These agglomerates resemble stacks where the platelets are placed directly on top of each other. In the cryo TEM micrograph of the same sample in Fig. 7(b), stacks of several platelets, lying in a lateral position, can be observed.
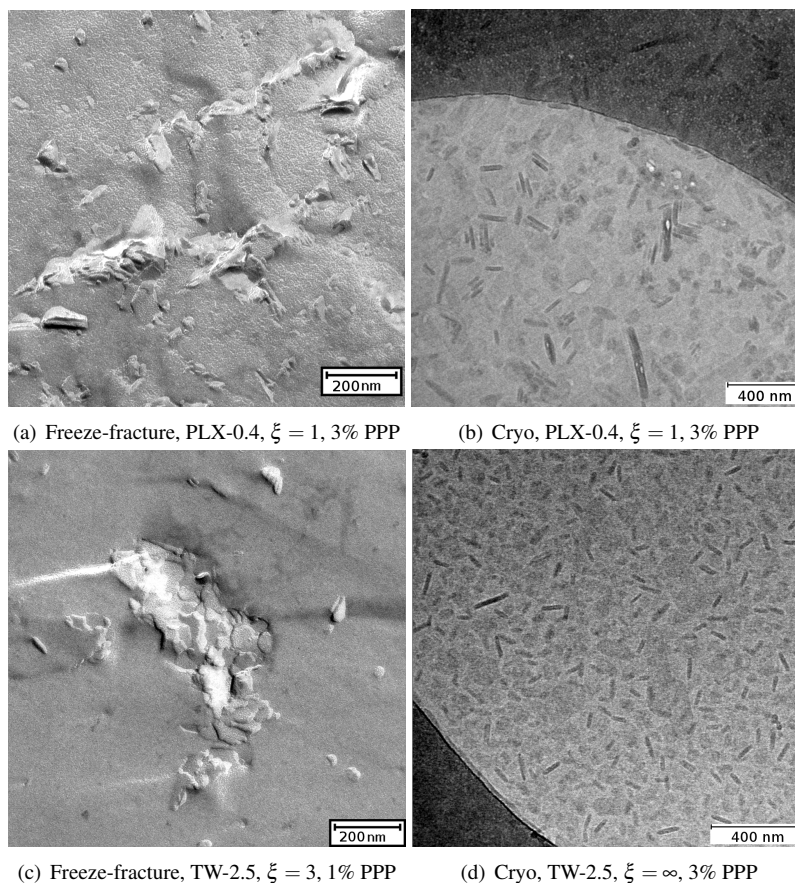

(a) Freeze-fracture, PLX-0.4, $\xi = 1$, 3% PPP   (b) Cryo, PLX-0.4, $\xi = 1$, 3% PPP

(c) Freeze-fracture, TW-2.5, $\xi = 3$, 1% PPP   (d) Cryo, TW-2.5, $\xi = \infty$, 3% PPP

Figure 7: Freeze-fracture TEM and cryo TEM micrographs taken from cLNP-DNA complexes prepared from different native PPP suspensions and charge ratios ξ.

A cLNP-DNA complex, prepared from TW-2.5 (1% PPP, $\xi = 3$), is visualized in Fig. 7(c). The complex with a size of about $600\,\text{nm}$ consists of many small platelets with diameters below $100\,\text{nm}$.

The micrograph suggests different local stacking directions, rather than just one. The cryo TEM micrograph in Fig. 7(d) provides a good representative overview over the platelets in the TW-2.5 suspension without DNA (3% PPP, $\xi = \infty$).

The cryo TEM micrographs in Figs. 7(b) and 7(d) suggest, as the PCS measure-

25

ments, a broad size distribution. Besides small platelets with diameters of less than 100 nm, also larger ones with typical sizes between 100 and 400 nm are found. The larger ones with a rather anisometric shape can be attributed to the stable β-PPP modification.[37] The smaller ones, which appear ubiquitously in the TW-2.5 suspension, are mainly associated with the unknown PPP modification.

In contrast to the smaller platelets, the larger ones preferentially align parallel to the frozen film surface in the cryo TEM micrographs and thus no information on their thicknesses can be obtained. To get at least some information on the smaller platelets, the thicknesses and diameters of 23 (PLX-0.4, Fig. 7(b)) and 61 (TW-2.5, Fig. 7(d)) small and clearly defined single or stacked platelets lying in a lateral position were analysed, respectively. Platelet diameters and thicknesses of 55.1 ± 18.6 nm and 12.2 ± 2.2 nm are found for PLX-0.4, 37.9 ± 8.9 nm and 10.6 ± 1.5 nm for TW-2.5. The reduced thickness for the small platelets in the TW-2.5 suspension with respect to those in the PLX-0.4 suspension agrees with the finding from the SAXS measurements of the native suspensions. The determined platelet diameters for the small platelets in the TW-2.5 suspension are comparable to the 25 - 30 nm reported by Bunjes *et al.* for the thin platelets in the unknown triglyceride modification.[29] These findings and the lack of any cLNP with a spherical morphology, which is characteristic for the α-modification,[37] support the idea that the pre-transitions in the micro-calorimetric heating runs and the changes in the WAXS diffractograms, which both rise with increasing DODAB concentration and using TW instead of PLX, are caused solely by the small and thin platelets of the unknown PPP modification.

3.3.3 SAXS measurements

The structure of the cLNP-DNA complexes on length scales between about 1 and 100 nm was probed by synchrotron SAXS. In particular it was studied if the cLNP platelets and the DNA form sandwich-like nanocomposites. The mean repeat distances d_{st} of the platelets in such sandwich structures are expected to be on the order of the platelet thicknesses of 10 - 20 nm.[21–24,30] This is much smaller compared to the 30 - 40 nm found for self-assembled platelet stacks in the native suspensions.

The SAXS patterns of the cLNP-DNA complexes, prepared from the native suspensions of the PLX-x series, feature 3 to 4 lamellarly ordered peaks (Figs. 5(b) to 5(f)). For complexes prepared from PLX-0.4, the peaks belong to a repeat distance of $d_{st} = 15.4$ nm, which is on the order of the platelet thicknesses. The magnitude of the peaks increases with decreasing charge ratio, but does not further grow, or even slightly decreases, when reaching the isoelectrical point $\xi = 1$.

The peaks of the lamellar order are strongly enhanced in the range of the 001 Bragg reflection. This clearly points to an interference between the scattering of the crystalline PPP platelets (001 Bragg peak) and the lamellar order. By this the SAXS data give strong evidence that the DNA can induce the formation of nanocomposites of stacked platelets with the DNA being at least partially condensed in between them.
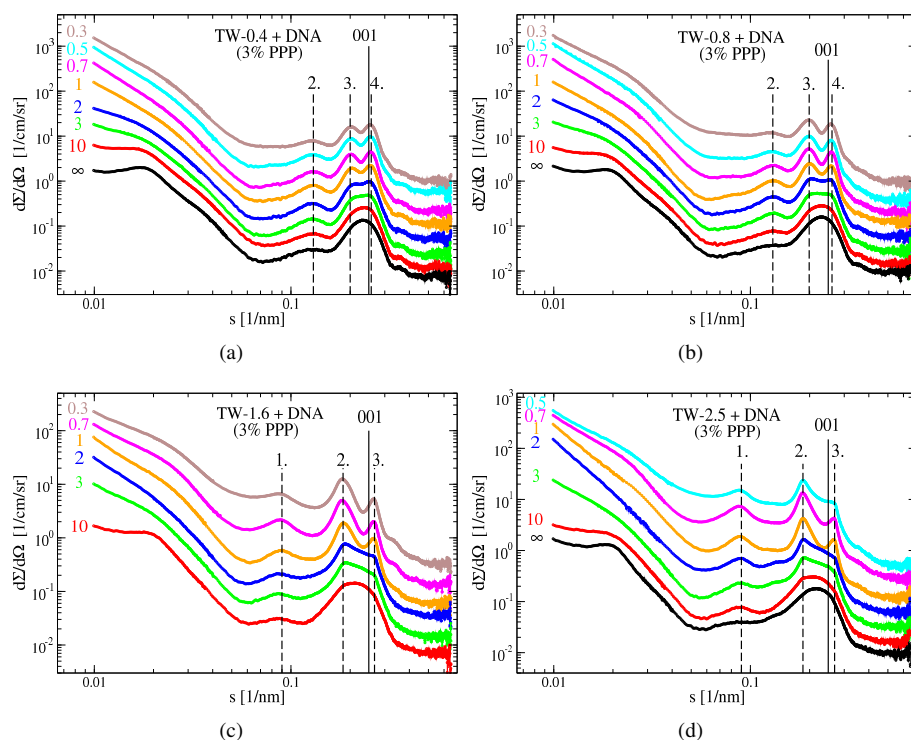

Figure 8: SAXS patterns (ID02 beamline) of cLNP-DNA complexes with charge ratios in the range ∞ (no DNA) to 0.3, prepared from the TW-x series: (a) TW-0.4 (3% PPP), (b) TW-0.8 (3% PPP), (c) TW-1.6 (3% PPP), and (d) TW-2.5 (3% PPP). For clarity, the SAXS patterns were scaled by multiples of 2 starting from the bottom. The position of the 001 Bragg reflection for bulk β-PPP and the first four orders of the stack-related interferences are marked by vertical lines.

In contrast to the stacks in the native suspensions, which are induced by an entropic effect for sufficiently large platelet concentrations, the nanocomposites are formed by electrostatic interactions between the DNA and the cLNP. While the stacks in the native PPP suspensions disintegrate upon sufficient dilution, the stacks of the cLNP-DNA complexes remain stable down to concentrations of 1% PPP, most probably for even lower concentrations. The small repeat distances in the cLNP-DNA complexes suggest that the PPP platelets lie directly on top of each other, with only the stabilizer molecules and DNA sandwiched between them.

The final concentration of the cLNP-DNA complexes has virtually no influence on the course of the patterns for $s > 0.03 \, \mathrm{nm}^{-1}$ (length scales $\lesssim 35 \, \mathrm{nm}$), when considering equal charge ratios (Figs. 5(b), 5(c) and 5(d) for PLX-0.4). The repeat distances ($d_{\mathrm{st}} = 15.4 \, \mathrm{nm}$) do not change with final PPP concentration and charge ratio since they solely depend on the thicknesses of the platelets in the native suspension. Only at lower s-values the patterns deviate from each other, which can be attributed to the interference of the scattering of different complexes as well as different complex sizes.

The SAXS patterns for the complexes with the PLX-0.4 suspension do not feature a 1st order interference of the lamellar order. Most probably the form factor of the nanocrystals (related to their thicknesses) is very small in the s-range of the first order ($s \approx 0.065 \, \mathrm{nm}^{-1}$), the interference with another scattering contribution such as Bragg or diffuse small-angle scattering is very limited in this range, too. The 3rd and 4th order interferences are enhanced due to the interference with the broadened 001 Bragg peak. The 2nd order interference at $s = 0.13 \, \mathrm{nm}^{-1}$ coincides with the broad halo around $s \approx 0.109 \, \mathrm{nm}^{-1}$ which is found in the SAXS patterns of the (native) PLX-0.4 suspension without DNA. With decreasing charge ratio, this bump gets slightly sharper and rises in intensity due to an interference with the stack-related scattering.

The stack-related scattering interference maxima for complexes with PLX-1.2 and PLX-2.0 are nearly at the same positions as those from PLX-0.4 (Figs. 5(e) and 5(f), Table SIII). However, when comparing same charge ratios, the peaks become much more intense. Even a 1st order can be clearly observed for charge ratios $\xi \leq 1$ (PLX-1.2) and $\xi \leq 3$ (PLX-2.0). This suggests a strongly enhanced formation of larger cLNP-

28

DNA complexes, when using suspensions with higher DODAB concentrations.

As for the native suspensions, no (PLX-2.0) and only a tiny bump (PLX-1.2) can be identified in the patterns without DNA. However, since the 1st order is always considerably lower than the 2nd one, there must be, as in the case of the complexes with PLX-0.4, another scattering contribution in the s-range of the 2nd order. Because of this interference effect, this contribution must be related to the (inner) structure of the platelets.

For complexes prepared from TW-0.4 and TW-0.8 (Figs. 8(a) and 8(b)), the situation is very similar as for the cLNP-DNA complexes obtained with the PLX-x series (in particular PLX-0.4). With increasing amount of DNA, a lamellar order with a repeat distance of 15.3 nm emerges. As for PLX-0.4, only the 2nd, 3rd and 4th orders are clearly visible. The latter two interfere with the 001 Bragg peak, the 2nd order at $0.13\,\mathrm{nm}^{-1}$ coincides with the position of the halo at $0.128\,\mathrm{nm}^{-1}$ which is found in the corresponding (native) suspensions without DNA.

The situation changes for the cLNP-DNA complexes prepared from TW-1.6 and TW-2.5 (Figs. 8(c) and 8(d)). The first three peaks of a lamellar order with a repeat distance of 11.2 and 11.1 nm, respectively, can be observed. This time, the 2nd and 3rd orders interfere with the 001 Bragg peak. Particularly for low charge ratios, the 001 Bragg peak becomes completely distorted. The 1st order can be observed at $s \approx 0.09\,\mathrm{nm}^{-1}$, since it interferes with the scattering of the bump at $s \approx 0.085\,\mathrm{nm}^{-1}$, found in the SAXS patterns of the (native) suspensions without DNA.

The lower repeat distance of about 11 nm for the complexes from TW-1.6 and TW-2.5 is in good agreement with the results for their corresponding native suspensions. As it was shown by PCS, WAXS, μDSC and TEM, TW-1.6 and TW-2.5 consist predominantly of the thin and small platelets of the unknown PPP modification, in contrast to PLX-x, TW-0.4 and TW-0.8, which are dominated by thicker and larger β-PPP platelets.
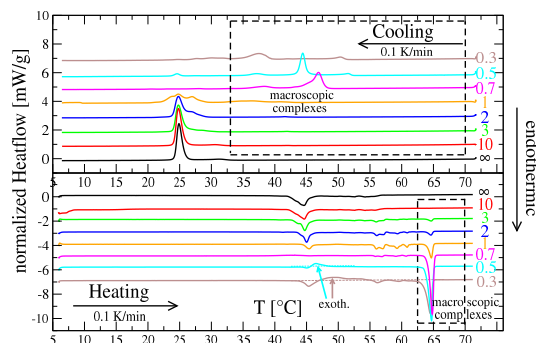
3.3.4 μDSC measurements

μDSC measurements were used to evaluate the agglomeration behaviour of the cLNP
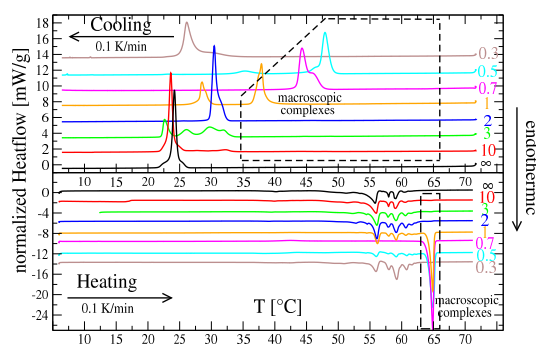
(a) PLX-0.4 + DNA (3% PPP)
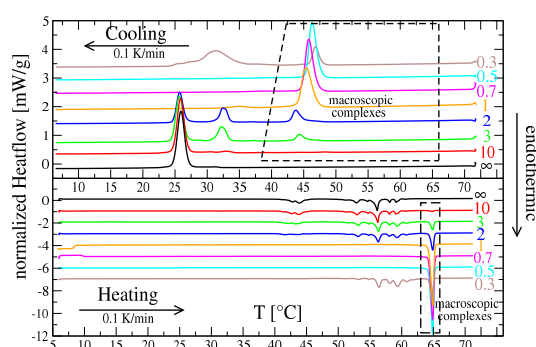
(b) PLX-1.2 + DNA (1% PPP)

(c) TW-2.5 + DNA (1% PPP)

Figure 9: μDSC heating and cooling runs for cLNP-DNA complexes prepared from different native suspensions and charge ratios in the range from ∞ (no DNA) to 0.3: (a) PLX-0.4 (3% PPP), (b) PLX-1.2 (1% PPP), and (c) TW-2.5 (1% PPP). For clarity, the curves were shifted vertically in steps of 2 mW/g (for a) and 1 mW/g (for b and c) with respect to the curve with charge ratio ∞. Dashed boxes mark the integration ranges for the melting and crystallization events caused by macroscopic cLNP-DNA agglomerates. The melting peaks at lower temperatures can be attributed to the melting and crystallization of small complexes consisting of only a few platelets and uncomplexed cLNP.

upon addition of DNA. As for PCS and TEM, complexes prepared from PLX-0.4, PLX-1.2 and TW-2.5 were studied.

The heating and cooling scans are visualized in Fig. 9. With decreasing charge ratio ξ a melting peak arises at temperatures in the range between $63\,^\circ$C and $66\,^\circ$C (*i.e.* around the melting point of bulk PPP of $66\,^\circ$C) in the heating runs. This peak can be attributed to the melting of (macroscopic) cLNP-DNA complexes consisting of many platelets. The enthalpy of fusion $\Delta H_{\text{fus}}^{\dagger}$ of this peak (integrated between 63 and $66\,^\circ$C, dashed box) and the total enthalpy of fusion ΔH_{fus} comprising all melting events in a heating run are listed in Table SIV in the Supplementary Material. The relative fraction of PPP in the macroscopic agglomerates with respect to the total amount of dispersed PPP was estimated by $\Delta H_{\text{fus}}^{\dagger}/\Delta H_{\text{fus}}$ and plotted in the middle part of Fig. 6. In good agreement with the PCS measurements, the formation of these large cLNP-DNA complexes rises considerably for $\xi \leq 2$.

The fractionated melting for temperatures below $63\,^\circ$C can be associated with the melting of small cLNP-DNA complexes, consisting of only one or a few platelets, and remaining uncomplexed cLNP platelets. Their contributions to the total enthalpy of fusion decreases to a minimum around the charge ratio $\xi = 0.7$, where virtually all complexes of the three investigated native suspensions become macroscopic in size.

Interestingly, for all three studied suspensions, the fraction of large complexes decreases for very low charge ratios, after reaching a maximum at 0.7 or 0.5 (*cf.* Fig. 6). This happens in particular for complexes prepared with low or moderate amounts of DODAB (PLX-0.4, PLX-1.2), while for complexes prepared from TW-2.5 the decrease is rather small. For complexes prepared from PLX-0.4, the fractionated melting peaks return for charge ratios of less than 0.7 in the temperature range below $63\,^\circ$C. At $\xi = 0.3$ the data suggests that virtually no large agglomerates are present any more. For these charge ratios the PCS measured hydrodynamic diameters were still in the micron range, however, as mentioned before, for charge ratios below $\xi = 0.7$, they also started to decrease.

The size of the complexes is correlated with their crystallinity. In the bottom part of Fig. 6 the total enthalpy of fusion ΔH_{fus} of the complexes (normalized by the PPP

concentration φ) is plotted as a function of the charge ratio. $\Delta H_{\text{fus}}/\varphi$ peaks between charge ratios 0.3 and 2 (maximum at 0.7), indicating an increased crystallinity of the agglomerated complexes.

The cooling runs support these findings. Complexes exhibiting melting contributions of large agglomerates in their heating run exhibit also crystallization events at high temperatures in their corresponding cooling run (the temperature range for the macroscopic complexes is marked by dashed boxes in the cooling runs of Fig. 9). Their enthalpies $\Delta H_{\text{cry}}^{\dagger}$ (integrated in the dashed boxes up to $66\,^{\circ}$C) and the total enthalpy of all crystallization events ΔH_{cry} in the cooling runs are listed in Table SIV. Since the ratios $\Delta H_{\text{cry}}^{\dagger}/\Delta H_{\text{cry}}$ and $\Delta H_{\text{fus}}^{\dagger}/\Delta H_{\text{fus}}$ in Fig. S6 in the Supplementary Material are virtually identical, the crystallization events in these high temperature ranges are clearly associated with the crystallization of the larger macroscopic complexes.

Small complexes and uncomplexed cLNP are associated with the crystallization events in the lower temperature range of the cooling curves. The former can be associated with the crystallization peak which appears at the same or a very similar temperature as for the DNA-free suspensions. The latter cause one or more additional crystallization events at slightly higher temperatures. Single platelets with adsorbed DNA or complexes consisting of only two platelets crystallize most probably at a very similar temperature as uncomplexed cLNP.

The cooling runs support the finding that complexes from PLX-0.4 with $\xi = 0.3$ and $\xi \geq 2$ are rather small, since they exhibit hardly any crystallization events linked to macroscopic complexes. For complexes prepared from PLX-1.2, the amount of macroscopic complexes for these charge ratios is significantly larger (*cf.* middle part of Fig. S6). For complexes from TW-2.5, the fraction of macroscopic complexes decreases considerably for $\xi \geq 2$, too. In contrast to the complexes from PLX-0.4 and PLX-1.2 it does not significantly decrease at very low charge ratios. PCS measurements of complexes from TW-2.5 revealed sizes in the micron range for $\xi \leq 2$ (top part of Fig. 6), too.

It is not surprising that the particle sizes for complexes from PLX-1.2 and TW-2.5 at the lowest charge ratio of 0.3 measured by PCS are still above 1 micron since a signif-

icant amount of macroscopic cLNP-DNA complexes is still present in the dispersions. For complexes from PLX-0.4 with $\xi = 0.3$ the situation is less clear, since hardly any macroscopic complexes were found by µDSC, but PCS indicated complex sizes above 1 micron. It is a matter of fact that even very small amounts of macroscopic particles can distort the PCS measured correlation function in a way that an overall large particle size is misleadingly computed for the PCS z-average.

For complexes from TW-2.5 and with charge ratios 0.3 and 0.5, the heating curves exhibit an exothermic event at about $46\,°C$ and $49\,°C$, respectively. They could be related to a phase transition of large agglomerates of platelets with the unknown PPP modification to the stable β-modification.

3.3.5 Replacing S100 by DMPC

In a next step the influence of the lecithin stabilizer on the morphology of the cLNP and the internal structure of the nanocomposites was investigated. For this purpose the lecithin blend S100 was substituted by the fully saturated lecithin DMPC in the native suspensions .
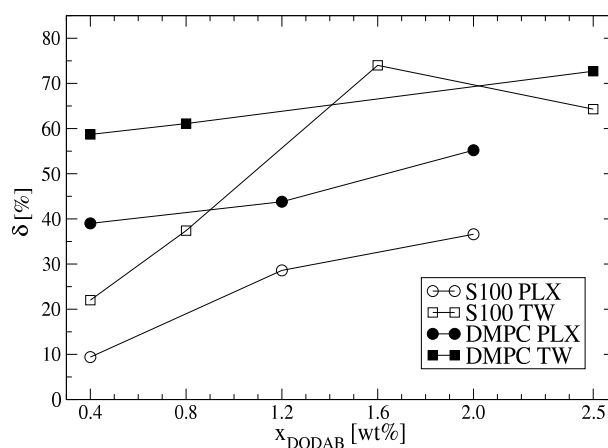

Figure 10: Fraction $\delta = \Delta H^*_{\text{fus}} / \Delta H_{\text{fus}}$ of the unknown PPP modification with respect to the total amount of dispersed PPP in the native suspensions for different DODAB concentrations and different combinations of the stabilizers S100 / DMPC and PLX / TW (data from Tables II and SIV).

As for their S100-stabilized counterparts the suspensions and their DNA-complexes

were analysed by PCS, μDSC, WAXS and SAXS. The most important findings are briefly described below, details can be found in part C.1 of the Supplementary Material. The fraction $\delta = \Delta H_{\text{fus}}^* / \Delta H_{\text{fus}}$ of the unknown PPP modification, as determined by μDSC (Tables II and SIV), is visualized in Fig. 10. As for the S100-stabilized suspensions, the amount of the unknown PPP modification grows with rising DODAB concentration at the expense the β-modification. Based on the μDSC and WAXS data, it can be concluded, that besides DODAB, also DMPC with its two saturated acyl chains, promotes the formation of the unknown PPP modification.

The SAXS patterns of the cLNP-DNA complexes revealed that now all native suspensions (*i.e.* not only TW-1.6 and TW-2.5 as for the S100-stabilized ones) produced nanocomposites with mean repeat distances d_{st} between 11 and 12 nm. This can be explained by the high fractions of platelets with the unknown PPP modification. Only for the DMPC-stabilized versions of PLX-1.2 and PLX-2.0 small traces of stacks with $d_{\text{st}} = 14.7$ nm were found.

From the analysis of the SAXS patterns of the native S100- and DMPC-stabilized suspensions (fraction δ of the unknown PPP modification; positions s_{b} of the form factor related bump(s) B (B$_1$ and B$_2$), Figs. 5(a) and S9(a)) and their cLNP-DNA complexes (repeat distances d_{st}), it turned out that δ, s_{b} and d_{st} are highly correlated via the platelet thicknesses.

As it is shown in Fig. S10 in the Supplementary Material and Fig. 10, a repeat distance of about 15 nm is always linked to a bump position between 0.11 and 0.13 nm^{-1} in the SAXS patterns and a small fraction $\delta \lesssim 40\%$ of the thin platelets of the unknown PPP modification. On the other hand, native suspensions with high fractions $\delta \gtrsim 55\%$ of the thin platelets feature bumps located between 0.083 and 0.092 nm^{-1} and produce always cLNP-DNA complexes with repeat distances between about 11 nm and 12 nm. For the transitional range $\delta = 40$ - 55%, the native suspensions feature both bumps, but their nanocomposites consist predominantly of the thinner platelets of the unknown PPP modification since the intensity of the stack-related peaks associated with repeat distances between 11 and 12 nm prevails those associated with repeat distances of about 15 nm (if they appear at all).

34

3.3.6 XNPPSA method

To further investigate the inner structure of the cLNP-DNA complexes, XNPPSA computer simulations were carried out and fitted simultaneously to the SAXS and SANS patterns of DNA-free ($\xi = \infty$) and DNA-loaded ($\xi = 1$) complexes prepared from the native S100-stabilized suspensions.

It is demonstrated that the XNPPSA-fits of stacked nanocrystals can reproduce the rather complicated SAXS and SANS patterns of the DNA-loaded complexes on an absolute scale. Thus, the SAXS and SANS patterns of the cLNP-DNA complexes are indeed the result of an interference between the scattering of the inner crystalline structure of the triglyceride platelets (001 Bragg peak), the scattering between the nanocrystals in the nanocomposites (stack-related, lamellarly ordered peaks) and the diffuse small-angle scattering (shape of the complexes and their platelets).

Case (1): Dilute suspensions without DNA (3% PPP, $\xi = \infty$)

The shell thicknesses were scanned in steps of 0.5 Å in the range $0.6 \leq d_{is} + d_{os} \leq 1.75$ nm with $0.4 \leq d_{is} \leq 1.55$ nm and $0.2 \leq d_{os} \leq 1.35$ nm for the simulated platelets in the diluted native suspensions (3% PPP, $\xi = \infty$). Each simulated dataset (combination of d_{is} and d_{os}) was fitted simultaneously to the SAXS and SANS patterns.

The SAXS and SANS patterns of the diluted versions of the PLX-x series and their best XNPPSA fits are visualized in Fig. 11. The fitted, discrete distribution of the volume fractions c_i of the nanocrystal thicknesses (given in numbers of d_{001}), EDs and NSLDs of the shells and dispersion medium are shown in Figs. 11(a) (PLX-0.4), 11(b) (PLX-1.2) and 11(c) (PLX-2.0). The best fitted values for the shell thicknesses d_{is} and d_{os} (along with the mean and variance values of all good fits) are listed in the legend of Fig. 11.

For the TW-x series (3% PPP, $\xi = \infty$) the SAXS patterns (SANS not measured) and their XNPPSA fits are plotted in Fig. S11 in the Supplementary Material and the fit parameters accordingly in Figs. S11(a) (TW-0.4), S11(b) (TW-0.8) and S11(c) (TW-2.5).

The fitted platelet thickness distributions (c_i) indicate that all suspensions are dominated by platelets with a thickness of 2 unit cells. The distributions shifts to smaller thicknesses with increasing DODAB concentration, where the number of platelets with a thickness of three and more unit cells decreases in favor of platelets with only one unit cell. For TW-2.5, nanocrystals with a thickness of one unit cell even outweigh those with two unit cells.

Remarkably, for PLX-0.4 and TW-x, the fits could even reproduce the bump in the SAXS and SANS patterns between the 001-Bragg peak and the onset of the diffuse small angle scattering. As already stated above, the bump must be related to the (inner) structure of the platelets. The fitted distributions of the platelet thicknesses support the idea that the bump is related to the form factor of the platelets, which is governed mainly by the thickness of the platelets in this s-range. While for PLX-0.4 (bump position $s_b = 0.11\,\text{nm}^{-1}$, Table SIII), and similarly for TW-0.4 and TW-0.8 ($s_b = 0.13\,\text{nm}^{-1}$), most platelets have a thickness of only two unit cells, for TW-2.5 ($s_b = 0.085\,\text{nm}^{-1}$) a large fraction of the platelets is one unit cell thinner in thickness. Besides small differences in the platelet thickness distributions, the small differences in s_b between PLX-0.4 and TW-0.4/0.8 could be related to differences in their shell thicknesses.

Case (2): cLNP-DNA complexes (3% PPP, $\xi = 1$)

The volume fraction of the stabilizers (*cf.* Table I: 7.9 - 9.5% for the PLX-x and 8.8 - 10.9% for the TW-x series) and their weight densities are very similar to the one of the PPP matrix (10%). Assuming, that all stabilizer molecules are adsorbed on the nanocrystals, the thickness $2 \cdot (d_{is} + d_{os})$ of the shells covering the platelets on its two large 001 faces could be similar to the mean thickness of the β-PPP nanocrystals.

The fits of the diluted native suspensions suggested, that the observed mean repeat distances d_{st} in the complexes of the PLX-x series (15.1 - 15.4 nm, *cf.* Table SIII) could stem predominantly from platelets with a thickness of two β-PPP unit cells ($2 \cdot d_{001} = 2 \cdot 4.02 \approx 8$ nm) plus a similar thickness of the stabilizer layers and the DNA
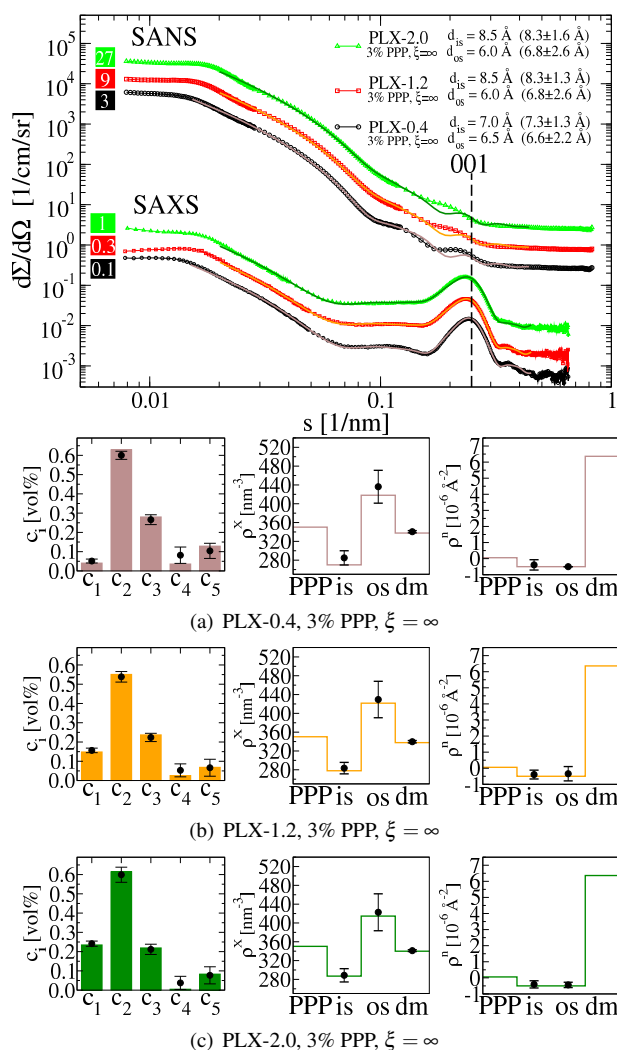
36

Figure 11: SAXS and SANS patterns of dilute suspensions of the PLX-x series (3% PPP, $\xi = \infty$). The XNPPSA fits are drawn as solid lines. The fitted platelet thickness distributions (coefficients c_i), electron densities (ρ^X) and neutron scattering length densities (ρ^n) of the inner and outer shell (is,os) and the dispersion medium (dm) are visualized, too. For a better visualization the patterns were multiplied by factors indicated on the left side of each curve.

between two nanocrystals. Therefore, for the complexes of the PLX-x series stacks of nanocrystals with a thickness of two β-PPP unit cells were simulated. The mean repeat distance of the nanocrystals in the simulated stacks was $d_{st} \pm \sigma_{st} = 15.4 \pm 0.25$ nm. The shell thicknesses were scanned in steps of 0.5 Å in the range $0.6 \leq d_{is} + d_{os} \leq 3.7$ nm with $0.4 \leq d_{is} \leq 1.4$ nm and $0.2 \leq d_{os} \leq 2.6$ nm, such that the total platelet thickness,
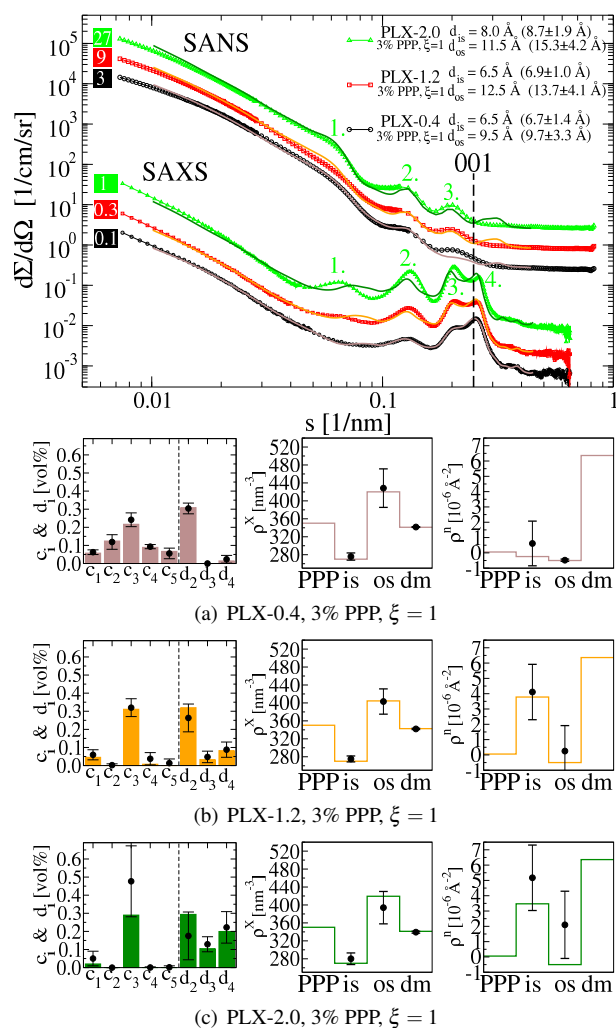
Figure 12: SAXS and SANS patterns of cLNP-DNA complexes formed with the PLX-x series (3% PPP, $\xi = 1$). The XNPPSA fits are drawn as solid lines. The simulated stacks consist of platelets with a **thickness of two unit cells PPP**. The fitted platelet thickness and stack size distributions (coefficients c_i and d_i), EDs (ρ^X) and NSLDs (ρ^n) of the inner and outer shell (is,os) and the dispersion medium (dm) are visualized, too. For a better representation the patterns were multiplied by factors indicated on the left side of each curve.

including the shells, $2 \cdot d_{001} + 2 \cdot (d_{is} + d_{os}) \lesssim 15.4$ nm, did not exceed d_{st}.

Besides stacks of up to four nanocrystals (each with a thickness of two β-PPP unit cells), single platelets with thicknesses of 1 - 5 unit cells of β-PPP were permitted in the fits. The SAXS and SANS patterns for the complexes of the PLX-x series (3% PPP,

38

$\xi = 1$) and their simultaneous XNPPSA fits are visualized in Fig. 12. For PLX-0.4 and PLX-1.2, the fits can reproduce the SAXS data very well. Deviations arise mainly in the range of the 001 Bragg reflection in the SANS patterns. Even the SAXS and SANS patterns of the complexes from PLX-2.0, exhibiting very strong interference patterns, can be essentially reproduced.

The corresponding fit parameters (volume fractions c_i of single platelets with thicknesses of 1 - 5 unit cells and d_i for stacks with 2 - 4 platelets per stack, EDs and NSLDs of the shells and the dispersion medium) are shown in Figs. 12(a), 12(b) and 12(c).

Discussion of the fit parameters

All fitted parameters should be considered only as approximations because of the complicated sample composition and the rather "simple" physical model of the platelets in the simulations.

First of all, only nanocrystals with the known high-resolution crystal structure of β-PPP were considered. However, for PLX-1.2, PLX-2.0 and the TW-x series, a significant or even predominant fraction of PPP is present in the unknown PPP modification.

Most probably, a fraction of the stabilizer molecules (in particular DODAB with its saturated acyl chains) can integrate with its hydrophobic part into the top layer of the PPP nanocrystals. The hydrophobic parts (e.g. PPG blocks in PLX vs. C_{16} and C_{18} fatty acid residues in S100 and DODAB) and hydrophilic parts (PEG blocks vs. phosphocholine head groups) of the stabilizer molecules are structurally very different. Thus, the simulation model as depicted in Fig. 2(c) with its sharp boundaries between the crystalline core, the two shells and the dispersion medium over-simplifies the problem.

The fitted values for the shell thicknesses d_{is} and d_{os} and the platelet thickness distribution (volume fractions c_i) should be considered only as an approximation.

Broadening of the 001 Bragg peak, potentially caused by the unknown PPP modification, defects in the crystals and the intercalation of the stabilizer molecules into the crystals are not considered in the model. Thus, the fitted thickness distribution might be shifted towards smaller thicknesses, than in reality.

The fitted EDs and NSLDs of the shells are often not consistent with a common model. In a previous study on the structure of the lecithin stabilizer layer of triglyceride nanocrystals, constraints between the EDs, NSLDs and thicknesses of the shells, based on a specific structural model of the lecithin head groups and acyl chains in the shells, were used in the fits. [21,22] However, for the samples studied here, this would be a challenging task because of the three different, interpenetrating stabilizer molecules (plus the DNA) in the shells.

The fitted size distribution of the stacks (number of platelets per stack d_i) for cLNP-DNA complexes can be correlated with the selected value for the variance of the repeat distances, σ_{st}. Higher and sharper stack-related inference maxima may result from both, a better order of the nanocrystals in the stacks (small σ_{st}), and a larger number of platelets per stack.

Another issue is the thickness of the nanocrystals in the nanocomposites.

With a thickness of $d_{001} = 4.02$ nm of one β-PPP unit cell, both, platelets with a thickness of two and three β-PPP unit cells would leave enough space (about 7 and 3 nm, respectively) for the stabilizer molecules and the DNA (the thickness of DNA in solution ranges between 2.2 and 2.6 nm [38]) in case of complexes with repeat distances of about 15 nm. For the fits of the complexes of the PLX-x series in Fig. 12, nanocrystals with a thickness of two unit cells were used, since they dominated the native suspensions (Fig. 11). However, simulations using stacks of nanocrystals with a thickness of three β-PPP unit cells (shell thicknesses scanned in the range $0.6 \leq d_{is} + d_{os} \leq 1.75$ nm with $0.4 \leq d_{is} \leq 1.55$ nm and $0.2 \leq d_{os} \leq 1.35$ nm, such that $3 \cdot d_{001} + 2 \cdot (d_{is} + d_{os}) \lesssim 15.4$ nm) provide fits (*cf.* Fig. S12 in the Supplementary Material), which are as good as those with stacks of platelets with a thickness of only two β-PPP unit cells. For the latter, the best fitted total platelet thicknesses in the stacks $2 \cdot d_{001} + 2 \cdot (d_{is} + d_{os})$ ranged with 11.2 - 12.0 nm clearly below d_{st}. For the former, the thicknesses $3 \cdot d_{001} + 2 \cdot (d_{is} + d_{os})$ of 15.2 - 15.6 nm were close to d_{st}. The thickness of 12.2 ± 2.2 nm, estimated by TEM for the fraction of small platelets in section 3.3.2, would support the idea of nanocrystals with a thickness of three unit cells in nanocomposites with a repeat distance of about 15 nm.

For complexes prepared from TW-1.6 and TW-2.5, the situation is complicated, too. The values of 11.1 - 11.2 nm for d_{st} differ almost exactly by the thickness of one β-PPP unit cell (4.02 nm) from those of the PLX-x series, TW-0.4 and TW-0.8. The fit of the native suspension TW-2.5 suggests mainly nanocrystals with a thickness of one and two unit cells PPP (*cf.* Fig. S11(c)). However, for complexes prepared from TW-1.6 and TW-2.5, it is not yet clear, whether the nanocrystals consist of one or two layers of PPP unit cells. The thickness of 10.6 ± 1.5 nm, estimated by TEM for the large fraction of the small platelets in TW-2.5, supports the idea of nanocrystals with a thickness of two unit cells in the nanocomposites. Indeed, simulations and fits carried out using stacks consisting of platelets with a thickness of two PPP unit cells (shell thicknesses $0.4 \le d_{is} \le 1.4$ nm and $0.2 \le d_{os} \le 1.2$ nm with $0.6 \le d_{is} + d_{os} \le 1.5$ nm, such that $2 \cdot d_{001} + 2 \cdot (d_{is} + d_{os}) \lesssim d_{st}$ where $d_{st} = 11.1$ nm and $\sigma_{st} = 0.2$ nm) can essentially reproduce the SAXS pattern for the cLNP-DNA complex ($\xi = 1$), prepared from TW-2.5 (*cf.* Fig. S11 in the Supplementary Material).

In summary, the XNPPSA simulations confirmed, that the platelet thicknesses decrease with increasing DODAB concentration in the native suspension. Furthermore, they support the idea, that the position of the bump is linked to the platelet thicknesses in the samples (form factor). More importantly, the XNPPSA fits proved that the lamellarly ordered maxima in the SAXS (and SANS) patterns of the cLNP-DNA complexes are caused by lamellarly assembled nanocrystals. However, a precise determination of the molecular arrangement of the stabilizer and DNA molecules between the nanocrystals, and the accurate thicknesses of the nanocrystals in the nanocomposites (2 or 3 unit cells in case of complexes for PLX-x), is not yet possible.

3.4   Suspensions without PPP

As a reference, triglyceride-free versions of PLX-0.4 and TW-2.5 were prepared by high-pressure homogenization and, along with their DNA-complexes, studied by SAXS. This was done, to rule out the possibility that unadsorbed stabilizers in the PPP suspensions could form structures with the DNA, causing the characteristic diffraction peaks (except the 001 Bragg peak for PPP) in the SAXS patterns of the cLNP-DNA

complexes.

A detailed description can be found in part C.3 of the Supplementary Materials. There it is shown that the SAXS patterns of these triglyceride-free DNA-complexes exhibit characteristic peaks, which do not match the interference maxima in the scattering patterns of the PPP-containing cLNP-DNA complexes. The SAXS patterns of the DNA-complexes with the stabilizer dispersions can be explained by multilamellar structures of mixed bilayers made from the stabilizers. An intercalation of the DNA in the water layer between the bilayers is very likely since similar sandwich-like structures were reported for DNA-complexes with the lecithin DOPC (1,2-dioleoyl-sn-glycero-3-phosphocholine) in the presence of divalent cations[39] and DNA-complexes with mixtures of DOPC with DOTAP.[17]

3.5   Final discussion

Depending on the DODAB concentration and the charge ratio, the complex sizes range from several hundred nanometers to macroscopic agglomerates of several microns. The former were found for low DODAB concentrations in the native suspension (e.g. PLX-0.4) high charge ratios. As demonstrated by PCS and micro-calorimetric measurements, larger platelet agglomerates increasingly formed, when the charge ratio ξ decreased from ∞ to the isoelectric point $\xi = 1$. Upon further addition of DNA ($\xi < 1$), the micro-calorimetric data (middle part of Fig. 6) indicated that the fraction of such large agglomerates reverts back to smaller values, at least for complexes, prepared from native suspensions with low amounts of DODAB (PLX-0.4 and PLX-1.2).

The observation of a maximum in the complex sizes at a charge ratio of about 0.7 (Fig. 6), and thus, close to the isoelectric point, would be in good agreement with similar observations in lipoplexes of DNA with cationic DODAB and DOTAP vesicles[40] and polyplexes of DNA with cationic polymers,[6] where a maximum agglomeration was found for charge ratios of 0.8 and 1, respectively.

The SAXS patterns in Figs. 5 and 8 exhibited only minor differences between patterns of complexes with the lowest charge ratios (0.3 or 0.5) and charge ratios close to the isoelectric point. Thus, despite a growing complex size / agglomeration, the num-
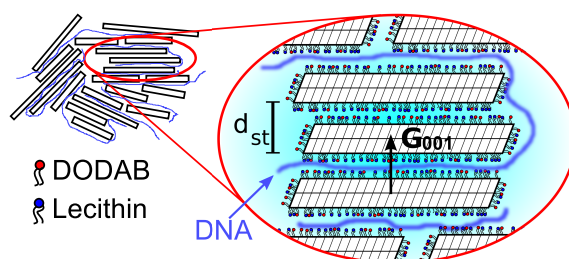
Figure 13: Structural model for complexes of DNA with the nanocrystalline triglyceride platelets with the DNA being intercalated between the platelets. The lecithin and DODAB molecules are indicated, poloxamer 188 / polysorbate 80 are omitted.

ber of the platelets in the stacks is nearly constant. This suggests, that larger complexes consist, as indicated in Fig. 13, of many small stacks with different stacking directions. This would be consistent with the results of the XNPPSA fits, where stacks of only a few nanocrystals could (essentially) reproduce the interference patterns. This effect cannot be attributed to a limited coherence volume, since for SAXS this is on the order of several $(100\,\text{nm})^3$, and thus, large enough to detect stacks consisting of several dozens of platelets.

The strong agglomeration for charge ratios close to and below the isoelectric point is a problem for most of the formulations presented here. Thus, the formulations and preparation method for the complexes must be improved, to achieve smaller sizes of the cLNP-DNA complexes. As it was demonstrated here, the choice of the stabilizers is an important control parameter. Suspensions with TW and DMPC produce significantly smaller and thinner platelets than suspensions stabilized by the combination of S100 and PLX. Furthermore, the size of the drug molecule / DNA that is to be sandwiched between the platelets might affect the complex size. The herring DNA strands in this study possess lengths in a broad range between 400 and 1000 base pairs[41] (own measurements with agarose gel electrophoresis (data not shown) showed lengths between about 100 and 3000 base pairs). With a length of 0.34 nm per base pair, the length of these DNA molecules is typically in the range of a few platelet diameters, and thus, the long DNA strands might promote the excessive agglomeration of the nanocrystals by a bridging effect.

43

As mentioned above, it was not possible to make definite conclusions on the DNA binding in the complexes from the XNPPSA fits to the SAXS and SANS patterns. The possibility, that unadsorbed stabilizer molecules in the suspensions form DNA-complexes, was ruled out with SAXS measurements of DNA-complexes prepared from equivalent triglyceride-free dispersions. First agarose gel electrophoresis measurements (data not shown) for complexes of the native suspension PLX-0.4 and PLX-1.2 proved the DNA binding in the complexes. For charge ratios below 1 (*i.e.* excess DNA) two fractions were identified. The first fraction of DNA remained bound within the complexes and stayed in the gel pockets. The second fraction was mobile DNA, which due its presence in excess in the samples, was not sufficiently bound in the complexes. For charge ratios above 1 the amount of mobile DNA decreased rapidly and only the first fraction of immobilized DNA was observed.

4 Conclusions

A route to prepare nanocomposites of DNA with platelet-like cationically charged triglyceride nanocrystals was presented. The native triglyceride suspensions were prepared by high-pressure melt homogenization using the cationic surfactant DODAB in combination with non-ionic stabilizers (lecithins and poloxamer 188 or polysorbate 80). The structure of the complexes was studied by X-ray, neutron and light scattering, TEM, micro-calorimetry and computer simulations from the atomic to the micron scale. In particular SAXS proved to be a reliable method to probe the structure of the nanocomposites at the nanoscale.

The observation of strong, lamellarly ordered peaks in the SAXS pattern of the cLNP-DNA complexes provided a strong evidence for stacks of lamellarly ordered platelets. Small-angle scattering pattern obtained with computer simulations using the XNPPSA method supported this finding. Moreover, reference SAXS measurements of complexes prepared from triglyceride-free dispersions (including only the stabilizers) could not reproduce the characteristic peaks in the SAXS data of their tripalmitin-containing counterparts.

Preliminary agarose gel electrophoresis measurements demonstrated that the DNA is immobilized in the complexes for charge ratios larger than the isoelectric point. For excess DNA (charge ratios $\lesssim 1$) a second fraction of mobile DNA was observed, which is not sufficiently bound in the complexes.

The choice of the nonionic stabilizers (DMPC vs. S100, TW vs. PLX) and high concentrations of the cationic stabilizer DODAB affected the morphology (diameter and thickness) and inner structure (triglyceride modification) of the nanocrystals. Increasing the DODAB concentration, using DMPC instead of S100 and TW instead of PLX promoted the crystallization of smaller and thinner platelets with an unknown triglyceride modification at the expense of the larger and thicker platelets of the β-modification. In this way, the inner structure of the nanocomposites (repeat distance of the nanocrystals) can be modulated with the stabilizer composition, too.

The size of the complexes was governed by the charge ratio between the platelets and the DNA (i.e. the ratio between the amount of DODAB and DNA). Suspensions with low amounts of DODAB and charge ratios not too close to the isoelectric point, produced predominantly small complexes, with only a small fraction of large agglomerates.

Acknowledgements

45

References

[1] B. Siekmann and K. Westesen, *Pharm. Pharmacol. Lett.*, 1992, **1**, 123–126.

[2] H. Bunjes, *Curr. Opin. Colloid Interface Sci.*, 2011, **16**, 405–411.

[3] C. Olbrich, U. Bakowsky, C.-M. Lehr, R. H. Müller and C. Kneuer, *J. Controlled Release*, 2001, **77**, 345–355.

[4] M. L. Bondì and E. F. Craparo, *Expert Opin. Drug Delivery*, 2010, **7**, 7–18.

[5] C.-H. Liu and S.-Y. Yu, *Colloids Surf., B*, 2010, **79**, 509–515.

[6] S. C. De Smedt, J. Demeester and W. E. Hennink, *Pharm. Res.*, 2000, **17**, 113–126.

[7] N. Pedersen, S. Hansen, A. V. Heydenreich, H. G. Kristensen and H. S. Poulsen, *Eur. J. Pharm. Biopharm.*, 2006, **62**, 155–162.

[8] K. Tabatt, M. Sameti, C. Olbrich, R. H. Müller and C.-M. Lehr, *Eur. J. Pharm. Biopharm.*, 2004, **57**, 155–162.

[9] K. Tabatt, C. Kneuer, M. Sameti, C. Olbrich, R. H. Müller, C.-M. Lehr and U. Bakowsky, *J. Controlled Release*, 2004, **97**, 321–332.

[10] G. Montana, M. L. Bondì, R. Carrotta, P. Picone, E. F. Craparo, P. L. San Biagio, G. Giammona and M. Di Carlo, *Bioconjugate Chem.*, 2007, **18**, 302–308.

[11] M. L. Bondí, A. Azzolina, E. F. Craparo, N. Lampiasi, G. Capuano, G. Giammona and M. Cervello, *J. Drug Targeting*, 2007, **15**, 295–301.

[12] A. Del Pozo-Rodríguez, D. Delgado, M. A. Solinís, A. R. Gascón and J. L. Pedraz, *Int. J. Pharm.*, 2007, **339**, 261–268.

[13] S. Bhattacharya and A. Bajaj, *Chem. Commun.*, 2009, 4632–4656.

[14] V. Chauhan, S. Singh, R. Kamboj, R. Mishra and G. Kaur, *J. Colloid Interface Sci.*, 2014, **417**, 385–395.

[15] R. Koynova and B. Tenchov, *Soft Matter*, 2009, **5**, 3187–3200.

[16] W. Yu, C. Liu, J. Ye, W. Zou, N. Zhang and W. Xu, *Nanotechnology*, 2009, **20**, 215102.

[17] J. O. Rädler, I. Koltover, T. Salditt and C. R. Safinya, *Science*, 1997, **275**, 810–814.

[18] G. W. Beall, D. S. Sowersby, R. D. Roberts, M. H. Robson and L. K. Lewis, *Biomacromolecules*, 2009, **10**, 105–112.

[19] K. Westesen, B. Siekmann and M. H. Koch, *Int. J. Pharm.*, 1993, **93**, 189–199.

[20] H. Bunjes and T. Unruh, *Adv. Drug Delivery Rev.*, 2007, **59**, 379–402.

[21] M. Schmiele, T. Schindler, T. Unruh, S. Busch, H. Morhenn, M. Westermann, F. Steiniger, A. Radulescu, P. Lindner, R. Schweins and P. Boesecke, *Phys. Rev. E*, 2013, **87**, 062316.

[22] M. Schmiele, T. Schindler, M. Westermann, F. Steiniger, A. Radulescu, A. Kriele, R. Gilles and T. Unruh, *J. Phys. Chem. B*, 2014, **118**, 8808–8818.

[23] M. Schmiele, S. Gehrer, M. Westermann, F. Steiniger and T. Unruh, *J. Chem. Phys.*, 2014, **140**, 214905.

[24] S. Gehrer, M. Schmiele, M. Westermann, F. Steiniger and T. Unruh, *J. Phys. Chem. B*, 2014, **118**, 11387–11396.

[25] T. Unruh, *J. Appl. Cryst.*, 2007, **40**, 1008–1018.

[26] A. Illing, T. Unruh and M. Koch, *Pharm. Res.*, 2004, **21**, 592–597.

[27] A. van Langevelde, K. van Malssen, F. Hollander, R. Peschar and H. Schenk, *Acta Crystallogr., Sect. B*, 1999, **55**, 114–122.

[28] C. Hoerr and F. Paulicka, *J. Am. Oil Chem. Soc.*, 1968, **45**, 793–797.

[29] H. Bunjes, M. H. J. Koch and K. Westesen, *Langmuir*, 2000, **16**, 5234–5241.

47

[30] T. Unruh, H. Bunjes, K. Westesen and M. H. J. Koch, *J. Phys. Chem. B*, 1999, **103**, 10373–10377.

[31] H. Bunjes, K. Westesen and M. H. Koch, *Int. J. Pharm.*, 1996, **129**, 159–173.

[32] H. Bunjes and M. H. J. Koch, *J. Controlled Release*, 2005, **107**, 229–243.

[33] E. Feitosa, R. D. Adati, P. Hansson and M. Malmsten, *PLoS ONE*, 2012, **7**, e44702.

[34] T. Unruh, K. Westesen, P. Bösecke, P. Lindner and M. H. J. Koch, *Langmuir*, 2002, **18**, 1796–1800.

[35] N. De Jaeger, H. Demeyere, R. Finsy, R. Sneyers, J. Vanderdeelen, P. van der Meeren and M. van Laethem, *Part. Part. Syst. Charact.*, 1991, **8**, 179–186.

[36] R. Finsy and N. De Jaeger, *Part. Part. Syst. Charact.*, 1991, **8**, 187–193.

[37] H. Bunjes, F. Steiniger and W. Richter, *Langmuir*, 2007, **23**, 4005–4011.

[38] M. Mandelkern, J. G. Elias, D. Eden and D. M. Crothers, *J. Mol. Biol.*, 1981, **152**, 153–161.

[39] D. Uhríková, M. Hanulová, S. S. Funari, R. S. Khusainova, F. Šeršeň and P. Balgavý, *Biochim. Biophys. Acta, Biomembr.*, 2005, **1713**, 15–28.

[40] J. C. Birchall, I. W. Kellaway and S. N. Mills, *Int. J. Pharm.*, 1999, **183**, 195–207.

[41] R. Dias, S. Mel'nikov, B. Lindman and M. G. Miguel, *Langmuir*, 2000, **16**, 9577–9583.